Multiple thermal AMOC thresholds in the intermediate complexity model Bern3D

Markus Adloff[1,2*], Frerk Pöppelmeier[1,2], Aurich Jeltsch-Thömmes[1,2], Thomas F. Stocker[1,2], Fortunat Joos[1,2]

[1] Centre for Environmental Physics, University of Bern, Switzerland

[2] Oeschger Centre for Climate Change Research, University of Bern, Switzerland

*Contact: markus.adloff@unibe.ch

Abstract

Variations of the Atlantic Meridional Overturning Circulation (AMOC) are associated with Northern Hemispheric and global climate shifts. Thermal thresholds of the AMOC have been found in a hierarchy of numerical circulation models, and there is an increasing body of evidence for the existence of highly sensitive AMOC modes where small perturbations can cause disproportionately large circulation and hence climatic changes. We discovered such thresholds in simulations with the intermediate complexity Earth system model Bern3D, which is highly computationally efficient allowing for studying this non-linear behaviour systematically over entire glacial cycles. By simulating the AMOC under different magnitudes of orbitally-paced changes in radiative forcing over the last 788,000 years, we show that up to three thermal thresholds are crossed during glacial cycles in Bern3D, and that thermal forcing could have destabilised the AMOC repeatedly. We present the circulation and sea ice patterns that characterise the stable circulation modes between which this model oscillates during a glacial cycle, and assess how often and when thermal forcing could have preconditioned the Bern3D AMOC for abrupt shifts over the last 788 kyr.

1 Introduction

The Atlantic Meridional Overturning Circulation (AMOC) transports warm waters from the Southern Hemisphere and the Mexican Gulf towards the Nordic Seas, until the gradually cooled salty water lost enough buoyancy and sinks, forming North Atlantic Deep Water (NADW). This water mass moves southwards along the western boundary of the Atlantic until it encounters the denser Antarctic Bottom Water (AABW) and slowly rises and upwells in the Southern Ocean, being ultimately incorporated either into AABW or the lighter Antarctic Intermediate Water (AAIW). The northward heat transport of the AMOC shapes regional climate by pushing the polar front north by several degrees of latitude, effectively

producing a climate in Europe and Greenland that is milder than predicted from latitude/insolation alone (Ruddiman and McIntyre 1981, Bard et al. 1987). It also affects global climate by shifting the Intertropical Convergence Zone (ITCZ) and monsoon systems (Wang et al., 2001, Bozbiyik et al, 2011), and interacting with the regional climate and deep water formation in the North Pacific (Okazaki et al., 2010, Menviel et al., 2012, Praetorius and Mix, 2014). The AMOC furthermore shapes biological surface productivity by regulating nutrient supply to the surface ocean in the Atlantic and Pacific (Tetard et al., 2017, Joos et al., 2017). On its southward path in the Atlantic, it influences deep ocean nutrient, carbon, and oxygen concentrations (Broecker, 1991). By affecting primary production and deep ocean carbon storage, AMOC changes also modulate atmospheric greenhouse gas concentrations (e.g. Menviel et al., 2008). Rapid changes in AMOC and hence Atlantic heat and carbon redistribution occurred repeatedly during the last glacial, termed Heinrich (Heinrich, 1988, Broecker, 1994) and Dansgaard-Oeschger events (Oeschger et al., 1984, Dansgaard et al., 1993), which had regional and global impacts on ecosystems and humans (e.g. Severinghaus et al., 2009, Timmermann and Friedrich, 2016). Yet, the factors determining AMOC stability are not fully understood.

As part of the thermohaline circulation, the AMOC is sensitive to both salinity and thermal forcing. Depending on the location of deep water formation in both hemispheres, the AMOC can switch between stable circulation states - either gradually or abruptly - as local vertical density profiles, sea ice extent, and meridional heat and salinity gradients change. Numerical experiments showed that large freshwater inputs into the North Atlantic can theoretically cause abrupt shifts from a vigorous circulation state to a temporarily subdued or collapsed circulation (e.g. Stocker and Wright, 1991, reviews by Weijer et al., 2019, Jackson et al., 2023). Such possible shifts of circulation state were first identified in box models (Stommel 1961) and confirmed in intermediate complexity models and global circulation models (Jackson and Wood, 2018, review in Jackson et al, 2023). Systematic testing of AMOC stability is done more easily in lower complexity models than General Circulation Models (GCMs), but the existence of multiple AMOC equilibria seems to be determined by the model-dependent existence and strength of feedbacks, with more complex models including more, possibly counteracting, feedbacks (Weijer et al., 2019). AMOC bistability could explain reconstructed sudden AMOC state shifts in the Pleistocene, possibly caused by large freshwater fluxes from melting continental ice shields and increased iceberg transport into the North Atlantic at the onset of Heinrich Events (Broecker, 1994, Grousset et al., 2000). Lags between the appearance of ice-rafted debris and the reconstructed cooling, however, suggest that freshwater fluxes could have instead acted as a positive feedback to AMOC weakening rather than triggering it (Barker et al., 2015).

76   Besides Heinrich event-like AMOC shifts to a less vigorous circulation in response to strong

77   freshwater forcing, there is increasing evidence for metastable AMOC states in-between the

78   glacial and interglacial circulation end-members. In some numerical models, and for narrow

79   parameter ranges (e.g. atmospheric CO_2 concentrations, ice sheet configurations), the

80   AMOC in such intermediate climate states is sensitive to small internal or external variability

81   and can sustain spontaneous oscillations (e.g. Aeberhardt et al., 2000, Knutti et al., 2002,

82   Zhang et al., 2014, Zhang et al., 2017, Brown and Galbraith, 2016, Vettoretti et al., 2022,

83   review of CMIP6 models in Malmierca-Vallet et al., 2023). Some of these oscillations could

84   be analogues to Dansgaard-Oeschger events that have been identified during intermediate

85   glacial climate conditions, specifically during Marine Isotope Stage (MIS) 3, and are thought

86   to be caused by internal feedbacks that amplified small changes of the North Atlantic salinity

87   balance (Zhang et al., 2014, Zhang et al., 2017, Vettoretti et al., 2022, Armstrong et al.,

88   2022). Meteoric and terrestrial freshwater input to the surface ocean are climate-dependent,

89   as is ice rafting and the salt rejection associated with sea ice formation. These processes

90   are thus impacted by, and impact themselves, the AMOC (Barker et al., 2015). Feedbacks

91   similarly exist for the salinity transport from the tropics to the North Atlantic, global circulation

92   patterns, and the salinity gradients which determine salt transport into the Atlantic basin

93   through the Bering Strait, Drake Passage, and from the Indian Ocean (e.g. Rahmstorf 1996).

94   Besides salinity changes, numerical experiments with GCMs also showed that the vertical

95   temperature profile affects AMOC stability (Haskins et al., 2020). Short-term AMOC

96   weakening in response to warming has been simulated by a wide range of GCMs (e.g.

97   Mikolajewicz et al., 1990, Gregory et al., 2005, Weijer et al., 2020). Thermal forcing of the

98   North Atlantic has also been found to cause longer term gradual changes in AMOC strength

99   in intermediate and higher resolution models (Manabe and Stouffer, 1993, Stocker and

100 Schmittner, 1997, Knorr and Lohmann, 2007, Zhang et al., 2017, Galbraith and Lavergne,

101 2019). In addition, bistability of AMOC under thermal forcing has been found in uncoupled

102 and coupled GCMs (Oka et al., 2012, Klockmann et al., 2018), and thermal forcing,

103 especially of the Southern Ocean, can cause abrupt AMOC state transitions similar to hosing

104 in the North Atlantic (Oka et al., 2021, Sherriff-Tadano et al., 2023). An important process in

105 the cooling-driven weakening of AMOC is the covering of former deep convection sites with

106 sea ice, which then causes a southward shift of deep convection (Oka et al., 2012). Such a

107 southward shift is only possible if the water column south of existing convection sites is

108 sufficiently destabilised by climate-driven density changes (Ganopolski and Rahmstorf,

109 2001).

110

111 So far, simulations of thermal AMOC thresholds have mostly been conducted with
112 computationally expensive numerical models, and the implications of the existence of AMOC
113 instability and thermal thresholds have not been tested across entire glacial cycles. While
114 providing crucial process understanding, direct comparisons of these simulations to proxy
115 records are therefore challenging.
116
117 Here, we demonstrate the existence of hysteresis and mode shifts in the AMOC in the
118 intermediate complexity model Bern3D, in the absence of freshwater hosing. Instead, we
119 only apply changes in the radiative forcing to the atmosphere-ocean system. We provide a
120 comprehensive description of the underlying processes and elucidate the influence of
121 radiative changes on the AMOC dynamics in the Bern3D model during orbitally-forced
122 glacial-interglacial cycles.
123
124   **2   Methods**
125
126 We employed the Bern3D intermediate complexity model version 2.0 (Müller et al., 2006,
127 Roth et al., 2014) to investigate the AMOC behaviour under a wide range of radiative forcing.
128 The Bern3D model comprises a 3D ocean component with a 40x41 horizontal grid and 32
129 depth layers, along with a 2D atmosphere (spatially-explicit energy-moisture balance with
130 prescribed wind fields) and dynamic sea-ice. The model explicitly calculates the thermo-
131 haline circulation with a frictional-geostrophic flow (Edwards et al., 1998) and contains
132 parameterizations to account for isopycnal diffusion and eddy-turbulence via the Gent-
133 McWilliams parameterization (Griffies, 1998). Temperature and salinity are dynamically
134 transported by the physical ocean model and respond to static seasonal wind fields and
135 changing atmospheric 2D energy and moisture balance, sea ice formation and external
136 forcings. Bern3D explicitly calculates Pacific-Atlantic transport through the Bering Strait, and
137 freshwater flux corrections are only imposed in the Weddell Sea, and compensated for in the
138 Southern Ocean to induce stronger deep water formation (Ritz et al., 2011, Roth et al.,
139 2014).
140
141 Table 1: Overview of the model experiments in this study. In set A, radiative forcing from
142 dust is scaled linearly with $\delta^{18}O$ and assuming different magnitudes at LGM as given in
143 parentheses.
144

Simulation Set	Simulation ID	Starting point and length	Forcing	Purpose
A	A0	MIS 19 spin-up 787500 years	orbital+GHG+dust(0 W/m²)	test AMOC changes in response to transient glacial-interglacial radiative forcing
	A1		orbital+GHG+dust(-1 W/m²)	
	A2		orbital+GHG+dust(-2 W/m²)	
	A3		orbital+GHG+dust(-3 W/m²)	
	A4		orbital+GHG+dust(-4 W/m²)	
	A5		orbital+GHG+dust(-5 W/m²)	
	A6		orbital+GHG+dust(-6 W/m²)	
	A7		orbital+GHG+dust(-7 W/m²)	
	A8		orbital+GHG+dust(-8 W/m²)	
B	B.slow	PI spin-up, 105 kyr	linear change in RF from 0 to -10 W/m² over 50 kyr and recovery over next 50 kyr	identify processes that cause AMOC shifts under radiative forcing
	B.slow.a	year 23000 of B.slow, 20 kyr	0.1 Sv freshwater input over 100 yr	test AMOC stability at different time steps in B.slow
	B.slow.b	year 24500 of B.slow, 20 kyr		
	B.slow.c	year 28500 of B.slow, 5 kyr		
	B.slow.d	year 47000 of B.slow, 5 kyr		
	B.fast.PI	PI spin-up, 25 kyr	linear change in RF from 0 to -10 W/m² over 10 kyr and recovery over next 10 kyr with different orbital parameters	test dependence of AMOC response to radiative forcing to orbital constellation
	B.fast.21ka	PI spin-up, 25 kyr		
	B.fast.30ka	PI spin-up, 25 kyr		
	B.fast.50ka	PI spin-up, 25 kyr		
	B.fast.80ka	PI spin-up with, 25 kyr		

We conducted two sets of simulations with the Bern3D model (Table 1). In set A, comprising nine simulations, we fully transiently simulated the last 788 kyr by imposing changes in orbital configuration, ice sheet albedo, and globally-averaged radiative forcing from the well-mixed greenhouse gases (GHG) CO_2 and CH_4 (combined here labelled as the 'standard forcing'). The runs started from an interglacial steady state (50 kyr with pre-industrial (PI) conditions and 2 kyr of re-adjustment to the radiative balance of MIS 19c). Orbital (Berger, 1978, Berger and Loutre, 1991), GHG (Bereiter et al., 2015, Loulergue et al., 2008, Joos and Spahni, 2008), and ice sheet albedo forcing (i.e. the standard forcing) is identical in each run (Fig. 1). Ice sheet albedo changes are calculated based on the benthic $\delta^{18}O$ LR04 stack (Lisiecki & Raymo, 2005) smoothed by averaging over a 10000-year moving window for the past 788 kyr.

The LR04 stack was chosen because it is the only complete record with constant temporal resolution over the simulated period. In our experiments, we applied spatially-uniform radiative forcings, to account for uncertainties in the glacial radiative balance, e.g. uncertain atmospheric optical depth changes due to changes in aerosols and dust, in addition to the better constrained temperature changes due to orbital changes and greenhouse gases, hence termed dust forcing. The scale of this forcing varies between the simulations and transiently within each simulation. The maximum radiative dust forcing, defined via the peak

166 LGM value in the smoothed $\delta^{18}O$ stack, is a free parameter, ranging from 0 to -8 W/m^2
167 relative to PI (Simulations A.0 to A.8). To construct the forcing, we scaled the maximum
168 forcing linearly with the smoothed LR04 stack, given the close correlation of reconstructed
169 dust fluxes and ice volume likely due to the dominant role of wind fields, sea level, and
170 hydrological cycle on dust fluxes (Winckler et al., 2008). The range of the resulting combined
171 radiative forcing is between -3 and -10 W/m^2. This range brackets estimates of maximum
172 reductions in global mean radiative forcing at the LGM of 7 - 8 W/m^2 due to albedo,
173 greenhouse gas, and aerosol effects (Albani et al., 2018). The imposed forcings resulted in
174 global mean surface temperature (GMST) differences between the LGM and PI of -3 to -9.6
175 °C. This temperature range encompasses most of the LGM-PI range reported in studies
176 investigating the Paleo Model Intercomparison Project (PMIP) 2, PMIP3, and PMIP4, which
177 range from -3.1 to -7.2 °C (Masson-Delmotte et al., 2013, Kageyama et al., 2021).

178

179 Furthermore, these simulations are also consistent with proxy-based reconstructions that
180 indicate GMST differences between -2 and -8 °C (Tierney et al., 2020), as well as covering
181 the -6.1 °C GMST difference as constrained by a recent data assimilation study with the
182 CESM model (Tierney et al., 2020). It is important to note that we only considered the
183 radiative effect of an assumed uniform distribution of aerosols in our simulations. In reality,
184 this distribution would be non-uniform and aerosols would have additional effects on
185 atmospheric freshwater fluxes, two factors which are both relevant for AMOC stability
186 (Menary et al., 2013) but are poorly constrained for the last 788 kyr. Furthermore, freshwater
187 fluxes associated with the build-up and disintegration of continental ice sheets and glaciers
188 were not taken into account in any of the simulations presented here. We also kept the
189 topography constant and do not close the Bering Strait during glacial states.

190

191 Simulation set B (Tab. 1) was designed to investigate the mechanisms behind radiation-
192 driven AMOC changes under more idealised boundary conditions. This simulation set
193 includes one long run with "slowly" changing radiative forcing (105 kyr, B.slow), five short
194 simulations with "fast" changing forcing (25 kyr, B.fast), and four simulations branched off
195 from B.slow at different points in time. B.slow started from a pre-industrial state, followed by
196 a linearly decreasing negative radiative forcing over 50 kyr, followed by a linear increase of
197 forcing back to the initial state also over 50 kyr (Figure 4). We continued the simulation for
198 an additional 5 kyr under constant, pre-industrial conditions to let the model re-equilibrate.
199 The setup of B.fast.PI is analogous to B.slow with the radiation decrease and consecutive
200 increase spanning 20 kyrs. The simulations started from a steady state with pre-industrial
201 orbital and GHG configuration, and were run with orbital configurations of PI, 21, 30, 50 and

202 80 kyrBP (simulations B.fast.PI, B.fast.21ka, B.fast.30ka, B.fast.50ka, B.fast.80ka,
203 respectively).

204

205 At four specific time points in B.slow, we branched off simulations to test the AMOC stability
206 by keeping all forcings constant, but at the same time applying a small freshwater hosing to
207 the North Atlantic (45°N-70°N) with a magnitude of 0.1 Sv over 100 years. If the AMOC is in
208 a stable mode i.e. far from a bifurcation point, it should recover from these freshwater
209 perturbations returning to its initial strength, while an unstable AMOC close to a bifurcation
210 point should transition into a new circulation mode.

211

212 We incorporated three passive circulation tracers ('dyes') in set B. Each of these dye tracers
213 is restored to 1 at the surface of a chosen region (Fig. SI.1), and to zero elsewhere in the
214 surface ocean, and has no sources or sinks below the surface. In the deep ocean, the dye
215 tracer concentration is hence diluted only by mixing with other water masses sourced from
216 other regions. These artificial dye tracers allow us to track the dispersal of North Atlantic
217 Deep Water (NADW), Antarctic Intermediate Water (AAIW) and Antarctic Bottom Water
218 (AABW) in the ocean interior.

219

220

221 **3   Results and Discussion**

222

223 We first investigate the response of the AMOC to changes in orbital configuration and
224 radiative forcing as transiently simulated in our 788 kyr-long simulations of set A. We aim to
225 provide a comprehensive understanding of radiation-driven AMOC dynamics on glacial-
226 interglacial timescales. Subsequently, we utilise the more idealised setup of simulation set B
227 to further examine the underlying mechanisms driving these changes in more detail.

228

229

230 **3.1. AMOC changes over the past eight glacial cycles**
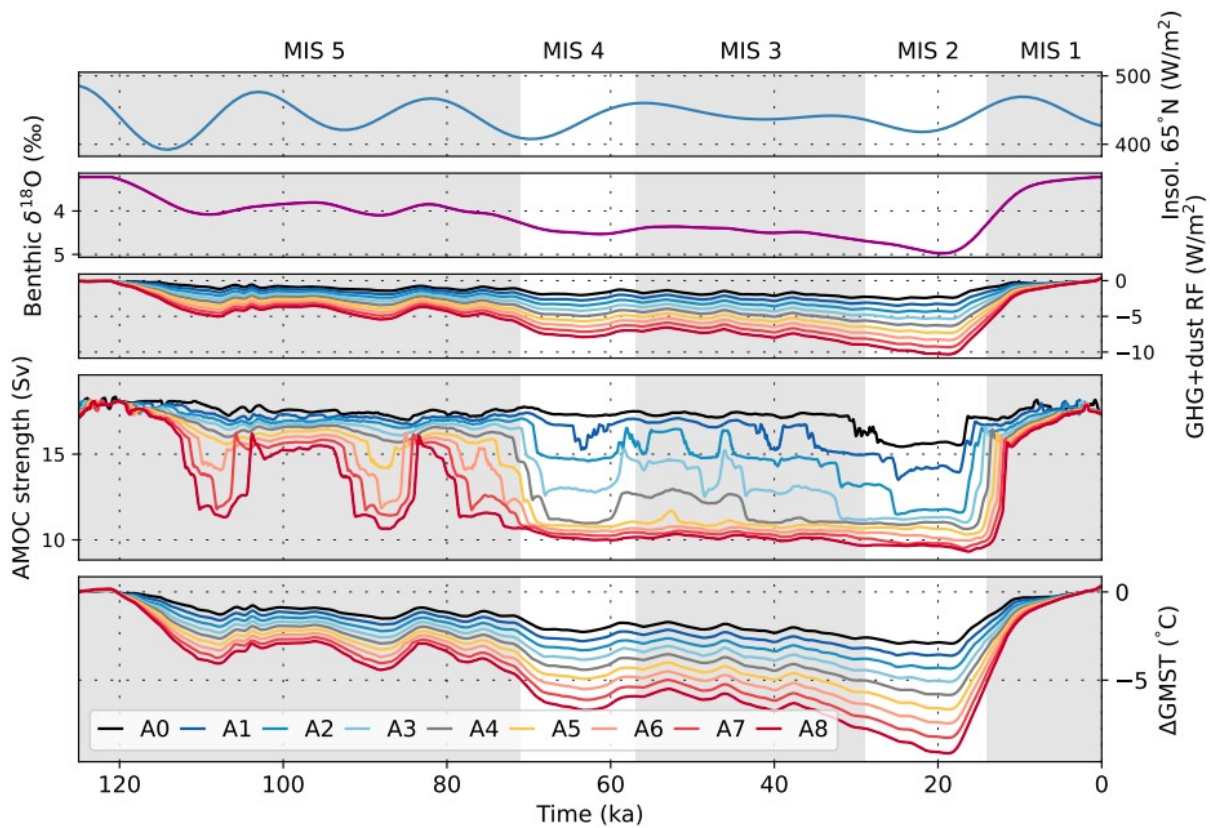
231

232 Figure 1: Forcings, AMOC and temperature response over the last 125 kyr of simulation
233 ensemble A. The upper three panels show July Insolation at 65°N, benthic $\delta^{18}O$ (10 kyr
234 spline of LR04, Lisiecki and Raymo, 2005) used to scale the dust forcing and the combined
235 effect of our dust forcing for each simulation and reconstructed atmospheric CO_2 changes
236 (Bereiter et al., 2015), smoothed with a second-order lowpass filter (cutoff frequency:
237 1/2000). The lower two panels show the 500 yr running mean of simulated AMOC strength
238 and GMST deviations from the PI in every simulation of simulation set A. Colours in the
239 lower two panels differentiate between simulations with different amplitudes of the radiative
240 forcing (see Methods).

241

242 In our simulations, radiative forcing- and orbitally-driven temperature changes resulted in
243 both gradual and abrupt AMOC shifts during each of the last eight glacial cycles (Fig. SI.2).
244 Fig. 1 illustrates the simulated AMOC threshold behaviour during these changes over the
245 entire last glacial cycle (past 125 kyr) with the different dust forcing scalings. Abrupt changes
246 in AMOC strength occurred in every simulation, with larger changes occurring under
247 stronger forcing. The magnitude of the dust forcing also determined the phase of the glacial
248 cycle during which the AMOC is most sensitive to radiative forcing: pronounced reductions in
249 radiative forcing under strong scaling resulted in a shift to the weakest AMOC mode early in
250 the last glacial cycle, which is from then on insensitive to further changes induced by
251 additional reductions in radiative forcing later on. Conversely, under weaker scaling, the

252 initial decrease in forcing was insufficient to shift the AMOC out of its interglacial circulation
253 mode.
254
255
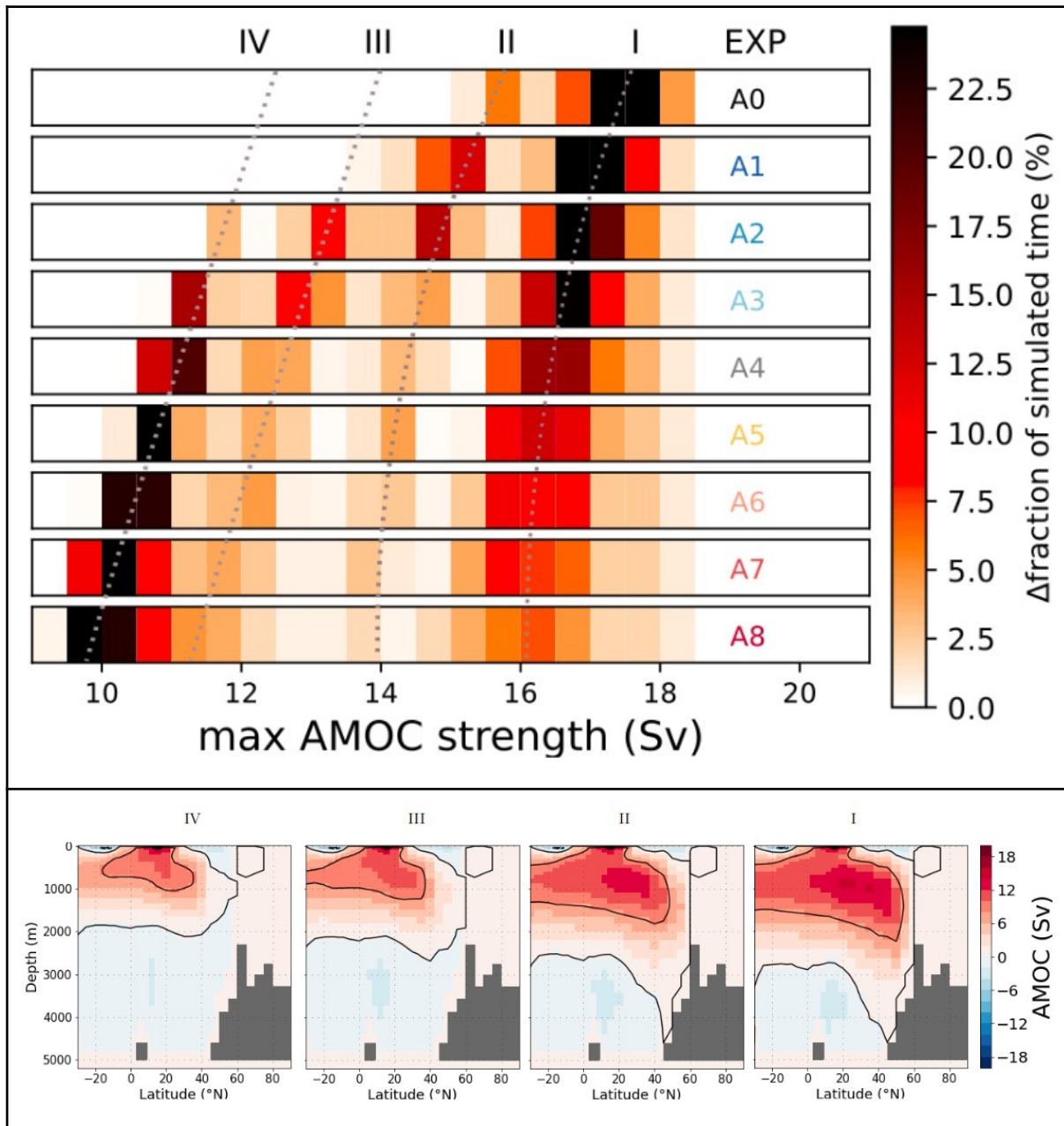
Figure 2: Top: Fraction of each simulation in simulation set A (each over 788 kyr) during
which a given maximum AMOC strength was simulated. Each row shows the results of one
simulation, with the simulation ID on the right end of the column in colours that correspond to
the lines in Fig 1. The bins are 0.5 Sv wide and four relative maxima in occurrence,
exhibiting distinct AMOC modes, $\mathrm{I} - \mathrm{IV}$, are indicated by dotted lines. Bottom: AMOC stream
function for the four circulation modes adopted across the last glacial cycle in simulation A3.
262

263 All simulations revealed multiple intermediate circulation modes between the glacial and
264 interglacial end-members. These modes manifested as distinct bands of increased
265 occurrence in Fig 2, which displays the fraction of the entire simulated period of 788 kyr
266 during which the AMOC exhibited a given maximum strength (binned into 0.5 Sv intervals).
267 The two intermediate modes II and III are distinguishable by AMOC strength, but not by their
268 meridional temperature or salinity gradients (Fig. SI.4), which questions whether these are
269 indeed separate circulation modes or expressions of one single mode that can have different
270 AMOC strengths (Lohmann et al. 2023). Yet, these circulation modes differ in global mean
271 and Greenland temperatures and North Atlantic Sea ice cover, suggesting that they are still
272 separate climate states (Fig. SI.5). Thus, we identified four frequently occurring circulation
273 modes in simulation set A that can be distinguished by AMOC strength, sea ice and
274 temperature, and three which can be distinguished by meridional temperature and salinity
275 gradients.
276
277 AMOC transitioned between these modes across the simulated glacial cycles due to
278 radiative forcing (Fig 2). The glacial and interglacial 'end-member' circulation modes I and IV
279 occured most commonly: The AMOC was in either of these two modes for 62-85% of the
280 simulated 788 kyr, depending on the dust forcing scaling. The AMOC was found in the
281 intermediate circulation modes II and III most commonly under weak dust forcing. For
282 stronger forcings, AMOC transitioned quickly through these modes, which were therefore
283 less frequently occupied. Thus, it appears that there is a tendency towards bi-modal AMOC
284 stability under strong forcing scaling, where the AMOC was almost exclusively either in the
285 glacial or interglacial circulation mode. Once AMOC had adopted the weakest mode,
286 additional reductions in radiative forcing only caused minor additional and gradual AMOC
287 weakening and did not cause another abrupt transition.
288
289 The simulations A3 and A4 with intermediate glacial-interglacial temperature changes (LGM-
290 PI ΔGMST -5 to -6 °C, similar to the -6.1 °C constrained by Tierney et al., 2020)
291 predominantly exhibited AMOC transitions between the interglacial (mode I, ~16-17 Sv) and
292 glacial mode (mode IV, ~11 Sv), with two rarer intermediate circulation modes in-between.
293
294
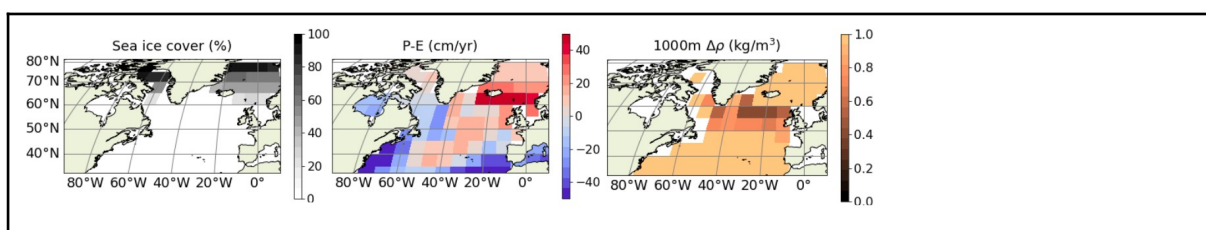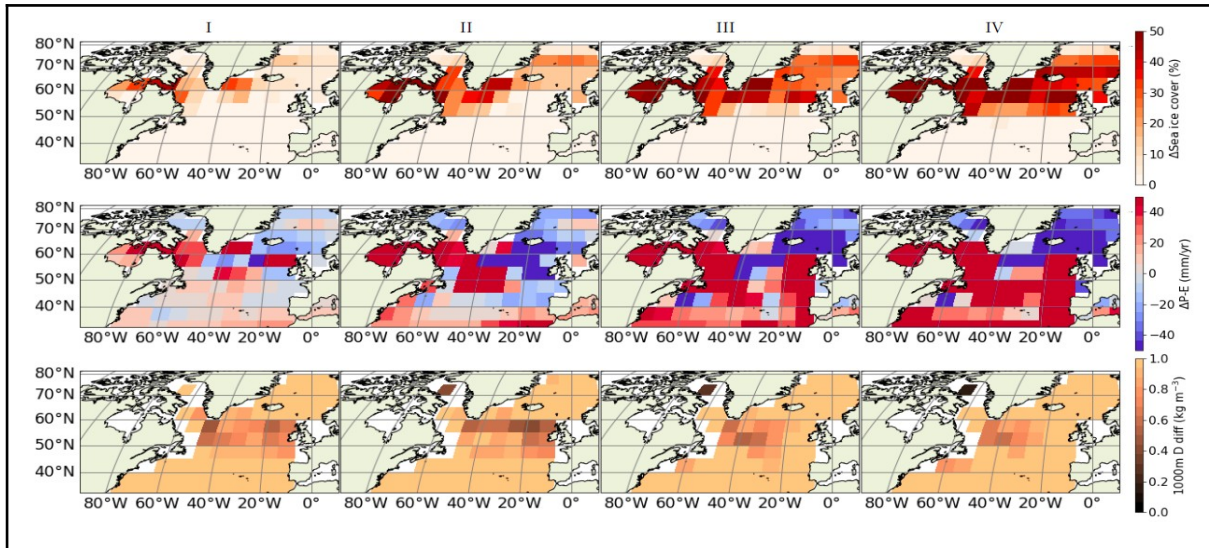
Figure 3: Initial annually averaged sea ice cover, meteoric freshwater balance, and the density difference over the uppermost 1000 m of the water column in the North Atlantic (upper panel). Changes of the annually averaged sea ice cover, meteoric freshwater balance, and the density difference over the uppermost 1000 m of the water column over the first 30 kyr of simulation B.slow in the lower panel.

The interglacial circulation mode (mode I in Figs. 2 and 3) is characterised by NADW formation in the subpolar North Atlantic, specifically south of Greenland and close to the British Isles, as indicated by the small density difference over the upper 1000 m of the water column. In the first intermediate AMOC mode (II), deep water formation is enhanced in the Eastern Atlantic while it weakens in the West as sea ice expands further South (Fig. 3). The next intermediate circulation mode (III) is marked by a reduction in deep water formation in the eastern North Atlantic, as the local water column increasingly stratifies. Deep water formation continues south of the sea ice edge in the western North Atlantic, albeit substantially weakened. As the northwards transport of subtropical water diminished under further cooling, the AMOC transitioned into the glacial stable mode (IV). In this mode, convection in the North Atlantic is strongly reduced and cold, fresh surface waters stratify the water column off the European coast. At this point, additional negative radiative forcing enhanced the amplitude of the temperature and salinity anomalies but without triggering additional changes in the North Atlantic circulation pattern.

Our simulations cover four glacial cycles before the Mid-Brunhes transition (MBT, MIS 12 and MIS 11 (~430 ka)) and four thereafter. This transition was marked by a shift to warmer interglacials with higher atmospheric CO_2 concentrations. There are only small differences between the distributions of AMOC modes before and after the transition (fig SI.2), and none

320 are statistically significant in the two-sided Smirnov test, which determines the likelihood that
321 two distributions are the same (Berger and Zhou, 2014), even at the 50% confidence level.
322

323 **3.2. Processes responsible for the AMOC changes**

324
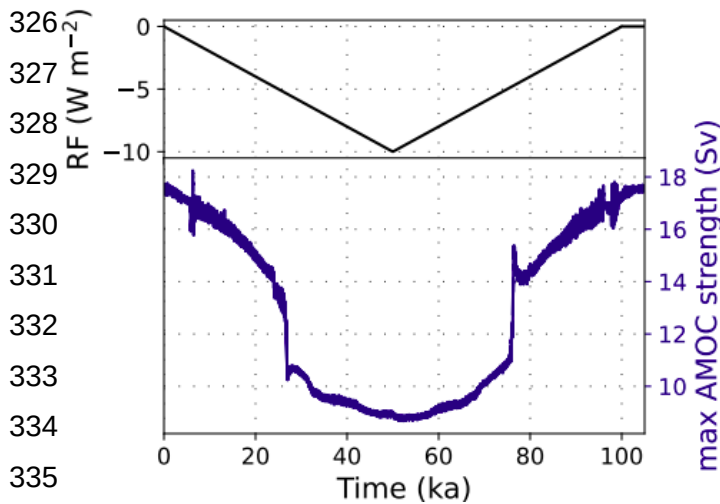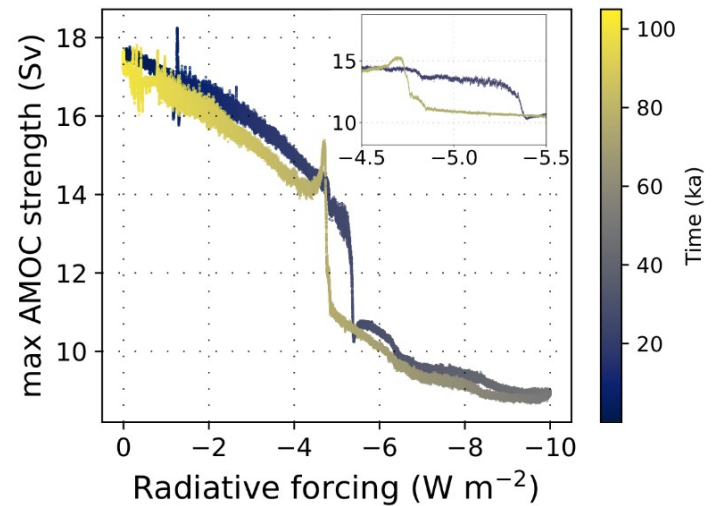
Figure 4: Simulation B.slow: (a) Response of the AMOC to changes in radiative forcing relative to the pre-industrial. The radiative forcing was linearly decreased over 50 kyr to a minimum of -10 W/m^2 and then increased again at the same rate. (b) The associated hysteresis loop of the AMOC under the radiative forcing, with the inset providing an enlarged view of the hysteresis loop.
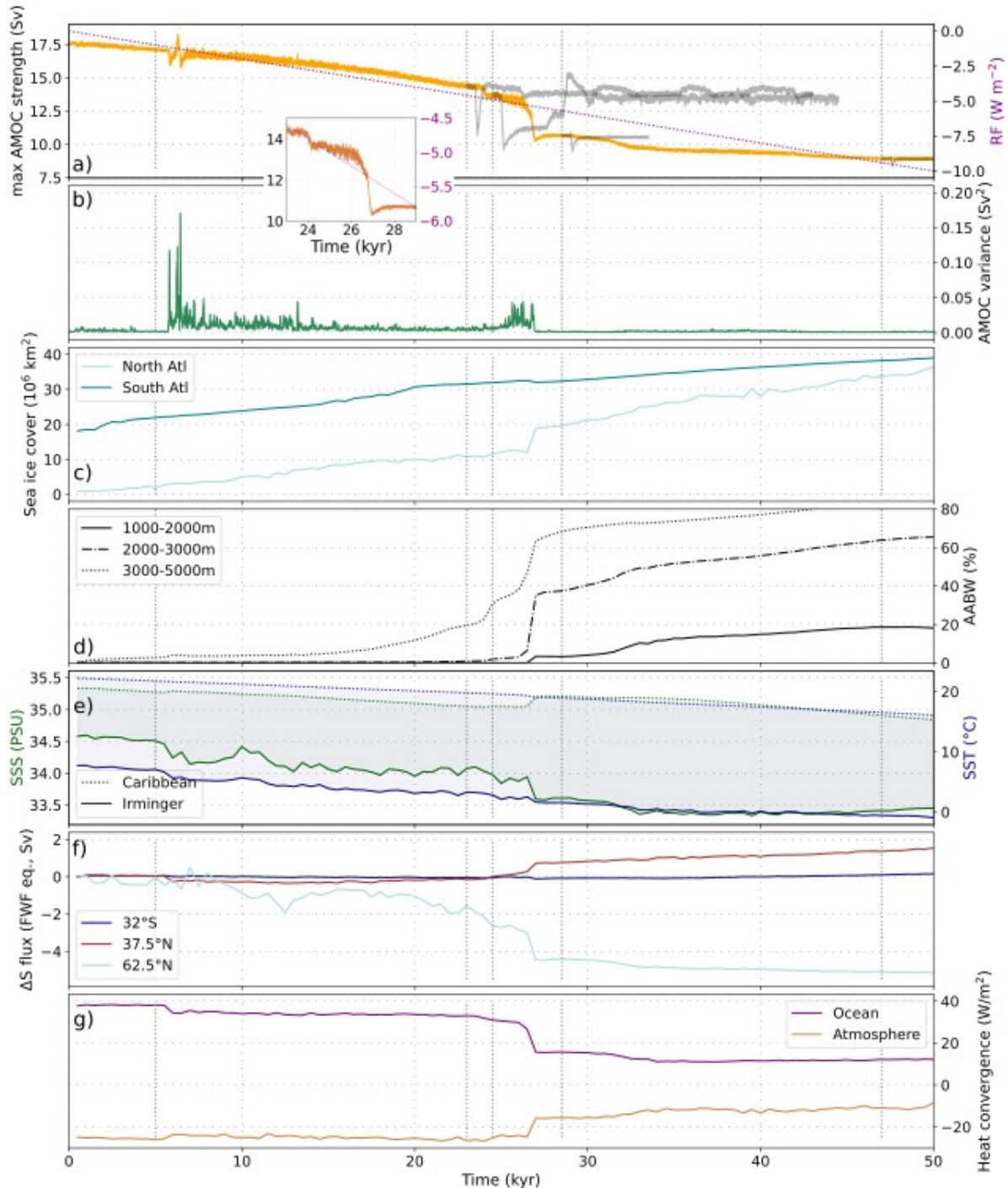
349

350   Figure 5: Changes in ocean properties during the cooling phase in simulation B.slow. a)
351   AMOC strength and the applied radiative forcing. At four points in time throughout B.slow,
352   simulations were branched off to test the stability of the respective circulation mode (shown
353   in dark grey). In these simulations, we kept the radiative forcing constant but applied a small
354   freshwater perturbation after 500 yrs, before allowing the model to re-equilibrate (see
355   Methods). b) AMOC variance calculated in a 50 yr moving window. c) Sea ice cover in the
356   North Atlantic between 50-60°N ('North Atl', light blue) and the Atlantic sector of the
357   Southern Ocean 50-68°S ('South Atl', teal). d) Volume fraction of AABW at three different

depth intervals in the subpolar North Atlantic (50-60°N). e) SST and SSS in the Caribbean and Irminger seas. f) Change in the northward salinity transport by ocean currents in freshwater flux (FWF) equivalents at different latitudes (following Liu et al., 2017). g) Column-integrated heat flux convergence due to ocean circulation and heat loss to the atmosphere (negative = heat loss by ocean) for the North Atlantic (40°N-70°N). Dotted vertical grey lines indicate time points in the simulation at which we branched off stability tests, and at which we analysed water mass distributions in Fig. 6.

In our simulations, the primary processes controlling the AMOC strength under changing radiative forcing are density changes due to heat and salinity redistributions. We investigated these in more detail in experiment B.slow (Fig. 4 and 5). This experiment is characterised by a slow linear decrease in radiative forcing over 50 kyr, before it is increased again to the pre-industrial value with the same rate of change (Fig. 4). Fig. 5 shows that AMOC weakened gradually over the first 24 kyr, then weakened abruptly by 1 Sv at 24 kyr into the simulation and by ~3 Sv at 27 kyr, and then continued to weaken gradually until the forcing is reversed (Fig. 5a). In addition to the abrupt transition in AMOC strength, we found several additional rapid changes in AMOC variability, heat, and salt fluxes (Fig. 5) and regional density profiles (Fig. SI.7-9) which were not associated with persistent changes in AMOC strength, e.g. at 6 kyr into the simulation. In fact, experiment B.slow shows that a cascade of changes with little effect on the mean AMOC strength occurred before the first abrupt AMOC weakening after 24 kyr. Since these changes might partially be artifacts of our coarse model resolution, we here only focus on the larger scale changes instead. Initially, the whole Atlantic surface ocean cooled and freshened, leaving the temperature and salinity differences between the Irminger and Caribbean Seas almost unchanged (Fig 5e). However, NADW became less salty and colder as a consequence of the changes in the surface ocean (not shown) and the vertical density profiles in the subpolar North Atlantic steepened due to the temperature and salinity changes (Fig. SI.7-8).

After about 6 kyr, the changes in the North Atlantic density profile shifted the location of NADW formation: NADW formation moved south as vertical density profiles in the subpolar east North Atlantic stabilised under a freshening of the surface and density profiles further south steepened due to surface cooling combined with subsurface warming (Fig. SI.7-9). These changes did not cause a step-change in AMOC strength, but freshwater and heat advection into the North Atlantic was reduced, sea ice expansion increased in the eastern North Atlantic, and AMOC variance (calculated over a moving 50-year window) was increased (Fig. 5). Transport of heat and salinity into the North Atlantic decreased (Fig. 5f, g), which reduced North Atlantic SST and SSS (Fig. 5e). The reduced influx of subtropical

395   surface waters also caused abrupt cooling and freshening in the Irminger Sea (Fig. SI.8). At
396   24 kyr, the AMOC had weakened to ~14.5 Sv and sea ice cover extended south of the
397   Irminger Sea (Fig SI.11). At this point, the AMOC strength dropped abruptly by 1 Sv, and
398   then by an additional 3 Sv ~3 kyr later, as the reduced salinity advection into the North
399   Atlantic and precipitation and evaporation changes led to a strong surface freshening. As a
400   result of the North Atlantic density changes, the main North Atlantic convection site shifted
401   southwards (determined by changes in the vertical density profiles, Fig SI.10). Sea ice also
402   increasingly covered former areas of deep water formation in the North Atlantic. In the
403   weakest circulation mode, the location of the maximum AMOC stream function shifted
404   southwards by approximately 10 degrees and up in the water column by 400 m initially (28.5
405   kyr) and eventually almost 800 m (47 kyr) This shift allowed cold, less dense water masses
406   to extend further south into the North Atlantic.

407

408   In the Southern Ocean, the cooling enhanced Southern Ocean deep water formation early
409   on in the experiment and led to a continuous expansion of sea ice in the Southern
410   Hemisphere. The biggest AMOC weakening at ~27 kyr was also accompanied by a weak
411   bipolar seesaw effect (Stocker and Johnsen, 2003), which caused a temporary decline in
412   sea ice coverage in the Atlantic sector of the Southern Ocean (Fig. 5). It was, however, too
413   small to reduce the radiation-driven sea ice increase in the longer term. Both shifts in AMOC
414   strength were accompanied by an increased spread of AABW into the North Atlantic (Fig.
415   5d).

416
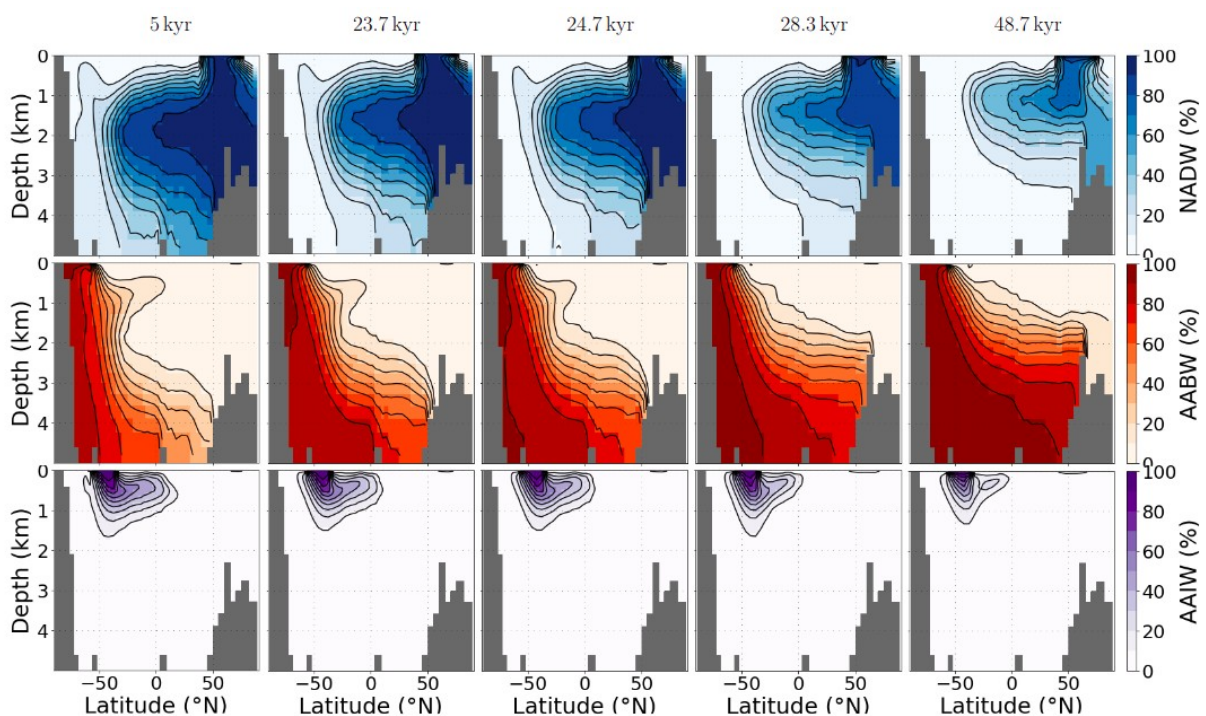
417

418   Figure 6: Atlantic water mass distributions at the five time slices of our simulation B.slow
419   indicated in Fig. 5. Each row shows the zonally-averaged contribution of water sourced in
420   one of three regions: the North Atlantic (upper row), the Southern Ocean (middle row), and
421   the Southern Atlantic (bottom row), diagnosed with three passive dye tracers. Fig. SI.1
422   shows the spatial pattern of our dye forcing.

423

424   The changes in the AMOC stream function associated with the decreasing radiative forcing
425   in experiment B.slow bear close resemblance to the changes we observed in the transient
426   experiment set A during AMOC transitions from the interglacial to the glacial circulation
427   mode (Fig. 6 and Fig. SI.12 - SI.14).

428

429   We tracked the effects of these circulation changes on the Atlantic distribution of
430   intermediate and deep water masses as diagnosed from artificial dye tracers (see Fig SI.1
431   for their source regions). Figure 6 shows that, during the first 23 kyr of our simulation, AABW
432   slowly spread further North and occupied increasingly shallower depths while the northward
433   reach of AAIW was reduced. Accordingly, NADW shoaled as it was unable to sink further
434   when encountering AABW in the deep North Atlantic. The reduced export of NADW also led
435   to a decrease in its southward extent, contracting to 40°S. The first abrupt shift in AMOC
436   strength occurred at 24.5 kyr in B.slow and had only small effects on the water mass
437   distribution. It mainly led to a reduced fraction of NADW at intermediate depths of the North
438   Atlantic >45°N and a small increase of AABW in the abyssal North Atlantic (Fig. 5d). The
439   following AMOC shift at 27 kyr reduced AMOC strength by more than 3 Sv, and was hence
440   also more strongly expressed in changes in the water mass distribution. It was accompanied
441   by a further reduction of NADW export into the deep Atlantic, before NADW was entirely
442   replaced by AABW at depths below ~3.5 km in the weakest circulation mode. AAIW was
443   increasingly curtailed in its northward reach, until it effectively no longer extended toward the
444   equator (<10%).

445

446   In summary, in our simulation deep convection diminished first in the Irminger Sea while
447   deep water formation continued in the subpolar Northeast Atlantic and south of Greenland.
448   As sea ice extended into the Eastern North Atlantic south of Greenland and vertical density
449   profiles steepened further south, the northward reach of the AMOC was restricted and a new
450   circulation mode was established with increased sea ice cover >55°N. The weakened
451   northwestward transport of heat and salt due to the reduced AMOC strength led to a
452   relatively fresh and cold eastern North Atlantic, stabilising the water column in the region and
453   producing another persistent AMOC mode. The simulated step changes in AMOC strength
454   in our simulations were thus the response to gradual surface cooling and freshening, and

455 occurred when NADW formation shifted southwards. The resulting redistributions of heat
456 and salinity caused sudden shifts in the vertical density profiles and sea ice expansion which
457 consolidated the new circulation mode (Ando and Oka, 2021). In particular, reduced
458 advection of heat and salinity into former locations of deep water formation resulted in a
459 more stable local water column (Fig. SI.7-9). The deep water formation regions are sensitive
460 to heat and salt flux changes, because any reduction in sea surface temperatures (SST)
461 increases surface density but simultaneously reduces evaporation in ice-free areas, thus
462 effectively creating a small freshwater forcing and a negative feedback to the buoyancy
463 changes caused by the initial SST decrease. Sea ice covering the downwelling areas
464 stabilises the water column by preventing surface ocean cooling and evaporation. The
465 progressive influx of AABW into the North Atlantic is a further process stabilising new
466 circulation modes by stratifying the water column from below (Buizert and Schmittner, 2015).
467 The difference between freshwater transport into the South Atlantic at 32°S and into the
468 Arctic at 62.5°N in Fig. 5f can be used as a measure for the basin-wide salinity feedback
469 (Rahmstorf, 1996, de Vries and Weber, 2005). In our simulation, changes in this metric were
470 predominantly caused by changes in the transport across the northern edge, since transport
471 into the South Atlantic remained almost unchanged throughout the cooling phase of B.slow.
472 North Atlantic salinity is instead governed by changing transport from the subtropics into the
473 North Atlantic and between the North Atlantic and Arctic. As such, the processes involved in
474 the sudden AMOC strength changes, namely density changes in the upper water column,
475 and those that stabilised new circulation modes (salinity and heat redistributions, sea ice
476 expansion) mostly operated in the North Atlantic region.
477
478 Our stability experiments demonstrated that the circulation modes before and after the
479 abrupt shifts recovered from small freshwater perturbations, and can thus be considered
480 stable, i.e. sufficiently far from bifurcation points to recover from the small perturbation (Fig.
481 5a, Fig. SI.6). In these branched off sensitivity tests, the circulation mode adopted before the
482 first AMOC threshold (at ~24 kyr), showed increased variability in the order of 0.5 Sv. The
483 next circulation mode (~25 kyr) responded most strongly to small freshwater perturbations
484 and was also the only circulation mode in our simulation which showed gradually increasing
485 AMOC variability (as determined by an increase in its variance) while approaching the next
486 threshold (Fig. 5a, Fig. SI.6). When the forcing was reversed, the radiation increase
487 gradually strengthened the AMOC until it rapidly transitioned back into the stronger
488 circulation mode when North Atlantic sea ice had receded sufficiently for a northward shift of
489 the convection sites and evaporation and salinity transport resumed. The radiative forcing at
490 which the AMOC transitioned from one circulation mode to the other was not equal for
491 decreasing and increasing radiative forcing: a stronger negative radiative forcing was

492 required to push the AMOC into its weak circulation mode than for the transition out of it (Fig.
493 4b).

494

495 Our sensitivity tests with different orbital configurations indicated that the existence of AMOC
496 thresholds under radiative forcing was not dependent on the initial orbital configuration.
497 However, the AMOC was slightly more sensitive to perturbations when initiated with the
498 orbital configuration equivalent to 30 ka before present. In this case, the threshold for the
499 AMOC to transition to its weaker mode was reached ~1 kyr earlier than under PI or 50 ka
500 orbital configurations (simulations B.short.30ka, B.short.PI, Fig. SI.15). The processes that
501 affected AMOC behaviour in simulation set B also caused AMOC changes over the
502 transiently simulated 788 kyr in simulation set A, but the circulation modes adopted varied
503 slightly in sea ice extent, hydrological cycle and salinity distribution under varying orbital
504 configurations.

505

506

507 **3.3. Comparison with other modelling studies and proxy data**

508

509 In our transient simulations covering the past 788 kyr, the AMOC strength decreased during
510 glacial phases solely due to changes in the hydrological cycle and sea ice that were induced
511 by orbital, greenhouse gas, and the additional radiative cooling. The existence of multiple
512 stable AMOC modes under varying thermal or radiative forcings has been found in various
513 GCMs (e.g. Knorr and Lohmann, 2007, Oka et al., 2012, Banderas et al., 2012, Brown and
514 Galbraith, 2016, Zhang et al., 2017, Klockmann et al., 2018). In agreement with previous
515 studies, we found multiple persistent AMOC circulation modes with distinct AMOC strengths
516 for radiative forcing levels between full glacial and interglacial climate states. Moreover, we
517 found that the transitions between these modes occur abruptly, some within as little as 100
518 years. In accordance with Lohmann et al. (2023), we found that these shifts in AMOC
519 strengths are preceded by cascades of density and circulation field changes, the number
520 and sequence of which depend on the strength of the forcing. Similar to the findings from
521 Oka et al. (2021), AMOC transitions arise primarily from salt redistribution in the ocean and
522 sea ice expansion into deep convection zones.

523

524 In our simulations, each transition in AMOC strength was associated with a shift in the
525 convergence of heat and salt fluxes and a southward expansion of sea ice into the North
526 Atlantic. Sea ice cover decouples the surface ocean buoyancy from the atmosphere. In the
527 intermediate modes, locations with steep density gradients are close to a critical annually-
528 averaged sea ice cover. In these modes, small changes in sea ice cover can cause large

529 changes in surface buoyancy and the extent and location of deep convection, which makes
530 the AMOC sensitive to small perturbations. The AMOC was only pushed into its weakest
531 mode when all former convection sites in the subpolar North Atlantic were sea ice-covered
532 and heat convergence in the North Atlantic was strongly reduced.

533

534 In their examination of thermal forcing of both hemispheres, Oka et al. (2021) found that
535 thermal AMOC thresholds only exist in COCO, the ocean component of MIROC, if the
536 Southern Hemisphere is cooled more than the Northern Hemisphere. In contrast, Zhang et
537 al. (2017) found sudden AMOC changes due to greenhouse gas changes without a special
538 focus on the Southern Hemisphere. In our simulations with Bern3D, we also found thermal
539 thresholds with similar cooling rates in both hemispheres, but only after salinity
540 redistributions and changing meteoric freshwater fluxes in response to about six thousand
541 years of global cooling.

542

543 It is possible that changing meteoric freshwater fluxes are essential for the existence of such
544 a thermal threshold, which does not therefore appear in an ocean model without a thermally
545 responsive atmosphere with a climate-driven freshwater balance. In a model with a dynamic
546 energy moisture balance component, atmospheric cooling reduces evaporation and the
547 water-holding capacity of the atmosphere. With this feedback enabled, cooling can then
548 affect seawater density directly via changing temperatures, and indirectly via changing the
549 meteoric freshwater balance and surface salinities. These changes would induce additional
550 kinematic changes (i.e., in the wind fields) in fully dynamic atmosphere models but are kept
551 constant in our simulations, i.e. the moisture content of air changes with climate but not the
552 direction or strength of winds which disperse it. In our model, a decrease in the water-
553 holding capacity of air therefore directly leads to a reduction of the large-scale atmospheric
554 moisture transport from low to high latitudes. Accordingly, wind stress fields are also kept
555 constant here. Changes in wind stress have been documented to exert important controls on
556 AMOC stability (e.g. Arzel et al., 2008, Yang et al., 2016) and thermal thresholds (Oka et al.,
557 2012). These effects have been investigated in detail with the Bern3D model by Pöppelmeier
558 et al. (2021) focusing on LGM boundary conditions.

559

560 The primary importance of salinity and heat redistributions as well as sea ice extent in the
561 North Atlantic for the simulated AMOC shifts resembles the findings from Ando and Oka
562 (2021)'s hosing experiments under LGM conditions and Zhang et al. (2017)'s simulations of
563 AMOC shifts in response to CO_2 changes under intermediate-glacial conditions. While our
564 experiments were run with pre-industrial topography, sea level and wind fields, the initial
565 location of convection sites between Greenland and the British Isles (areas with lowest

566   density differences over upper 1000 m in Fig. SI.11) resembles the LGM and intermediate-
567   glacial circulation modes in Ando and Oka (2021) and Zhang et al. (2017).

568

569   Ganopolski and Rahmstorf (2001) found that the possibility of a southward shift of deep
570   convection depends on the latitude of prior deep convection and the density field further
571   south, and Oka et al. (2012) showed that the location of deep convection and its distance
572   from the winter sea ice edge define thermal thresholds in AMOC strength. Several controls
573   on the location and strength of deep convection in the North Atlantic, that would have
574   affected AMOC stability over glacial cycles, have been established. The location of deep
575   convection is dependent on wind fields, climate and sea level/bathymetry (Ganopolski and
576   Rahmstorf, 2001, Oka et al., 2012, Zhang et al., 2017), and thus the thermal AMOC
577   thresholds are model and forcing dependent (Oka et al., 2012). Our simulations capture the
578   albedo effect of varying terrestrial ice sheet extent, but we did not consider their orography
579   or sea level effects, including impacts on the atmospheric circulation, which were shown to
580   affect AMOC (Li and Born, 2019; Pöppelmeier et al., 2021). Previous studies suggested that
581   pre-industrial or intermediate glacial ice sheet configurations are required to even produce a
582   thermal AMOC threshold in the range of glacial-interglacial CO_2 concentrations in a full GCM
583   and that the presence of a full glacial Laurentide ice sheet prevents such a threshold (e.g.
584   Klockmann et al., 2018). In addition, changes in the interconnection of marine basins,
585   specifically the Bering Strait, also affect AMOC stability (Hu et al. 2012). The values of the
586   thermal thresholds in our experiments are thus likely sensitive to the model design and
587   initiation. Pöppelmeier et al. (2021) showed that the sensitivity of Bern3D to freshwater
588   hosing increases when additional LGM boundary conditions are prescribed (changed wind
589   fields, closed Bering Strait, tidal mixing differences due to sea level changes). The different
590   wind fields and tidal mixing strengthened AMOC and increased the salt and heat transport
591   into the subpolar North Atlantic. This could mean that stronger cooling is required to stabilise
592   the water column in the Irminger Sea and reach the first thermal threshold, when the full
593   range of glacial boundary conditions are applied. Closure of the Bering Strait increased the
594   salt advection feedback, which stabilises the weak circulation state without deep water
595   formation in the subpolar North Atlantic.

596

597   Further investigations are needed to determine how changes in strength and location of the
598   wind stress due to the ice sheet's orography, sea level and Bering Strait closure would affect
599   sea ice formation in the northern North Atlantic and the AMOC thresholds in our simulations
600   quantitatively. Since we chose to focus on radiation driven AMOC changes in our
601   experiments, we would not expect a close model-data match with reconstructed AMOC
602   changes from paleo-records. Our simulations show that the reconstructed temperature

603 changes had the potential to alter the density field in the North Atlantic by redistributing heat
604 and salt, and that some of these changes might have resulted in abrupt changes of AMOC
605 strength. By testing a wide range of glacial-interglacial temperature changes, our
606 experiments demonstrate that the cooling during glacial periods likely contributed to a
607 weakened AMOC. The strength and timing of the weakening depends on the actual
608 temperature change in the North Atlantic which would have been modulated by changes in
609 winds and ice shields.
610
611
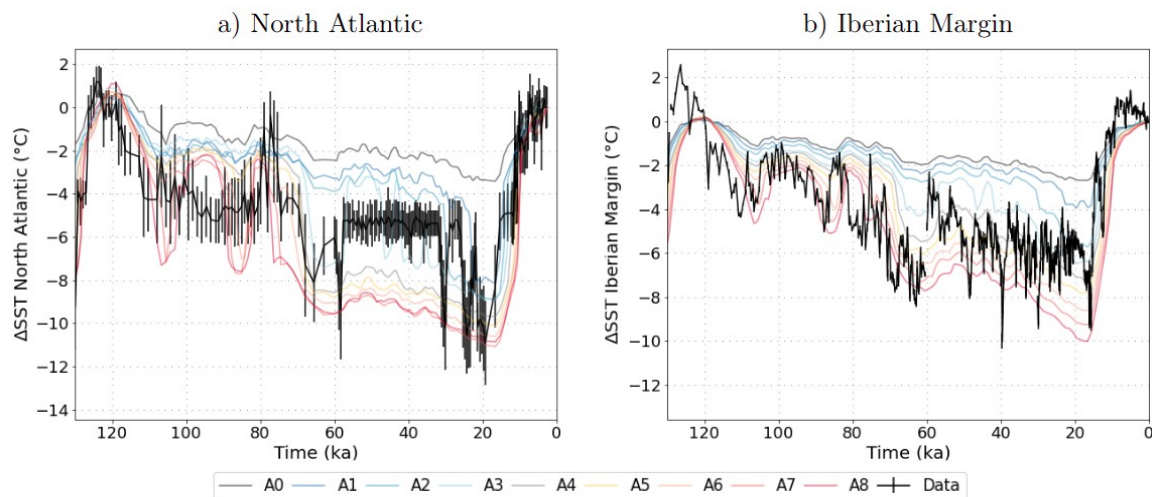
617 Figure 7: Simulated and reconstructed SST differences from PI over the last glacial cycle in
618 the North Atlantic (a, reconstruction by Candy and Alonso-Garcia, 2018) and on the Iberian
619 Margin (b, reconstruction by Davtian and Bard, 2023). The model data was interpolated to
620 the time points for which proxy reconstructions exist.
621
622 Unlike in our simulations, most GCMs participating in PMIP4 do not show a shoaling or
623 weakening of the overturning cell under LGM boundary conditions (Sherriff-Tadano and
624 Klockmann, 2021). The difference could arise from the static wind fields that we prescribed,
625 since an ice-sheet related increase in wind speeds over the North Atlantic leads to a
626 strengthened AMOC (Klockmann et al., 2018), or different representations of processes
627 affecting AABW density changes (e.g. brine rejection, Bouttes et al., 2011). A shallower and
628 likely weaker AMOC during peak glacials is however consistent with observational data
629 (Lynch-Stieglitz et al., 2017, Pöppelmeier et al., 2023). In Fig. 7, simulated SST changes
630 from the Rockall Trough and the Iberian Margin are compared to proxy-based
631 reconstructions. Circulation changes alter the distribution of heat in the North Atlantic, and
632 simulated SST patterns are strongly affected by AMOC changes. In response to the
633 stepwise AMOC weakening, simulated Atlantic SST also transitioned stepwise from
634 interglacials to glacial maxima. Step changes are also an established feature of Atlantic SST

635 reconstructions over the last glacial cycle (Fig. 7), with the biggest steps at 120-110 ka and

636 80-60 ka also captured in our simulations. During glacial inception between 120 ka and 70

637 ka, the amplitudes of reconstructed SST changes in both locations resemble those simulated

638 with strong radiative forcing (simulations A6, A7, A8). Afterwards, SSTs in those simulations

639 decreased more than in the reconstructions, and the latter align more closely with weaker

640 radiative forcing (simulations A3, A4). After ~70 ka, shorter millennial-scale events (Heinrich

641 and Dansgaard-Oeschger), that were not included in our simulations, were more frequent

642 than before and could affect the comparability between reconstructed and simulated SST.

643 Additionally, the further into the glacial cycle, the more the topography and wind fields would

644 have deviated from their pre-industrial states that we kept constant throughout the

645 simulations. These factors could have caused a shift in AMOC and SST changes that are

646 not captured by our simulations.

647
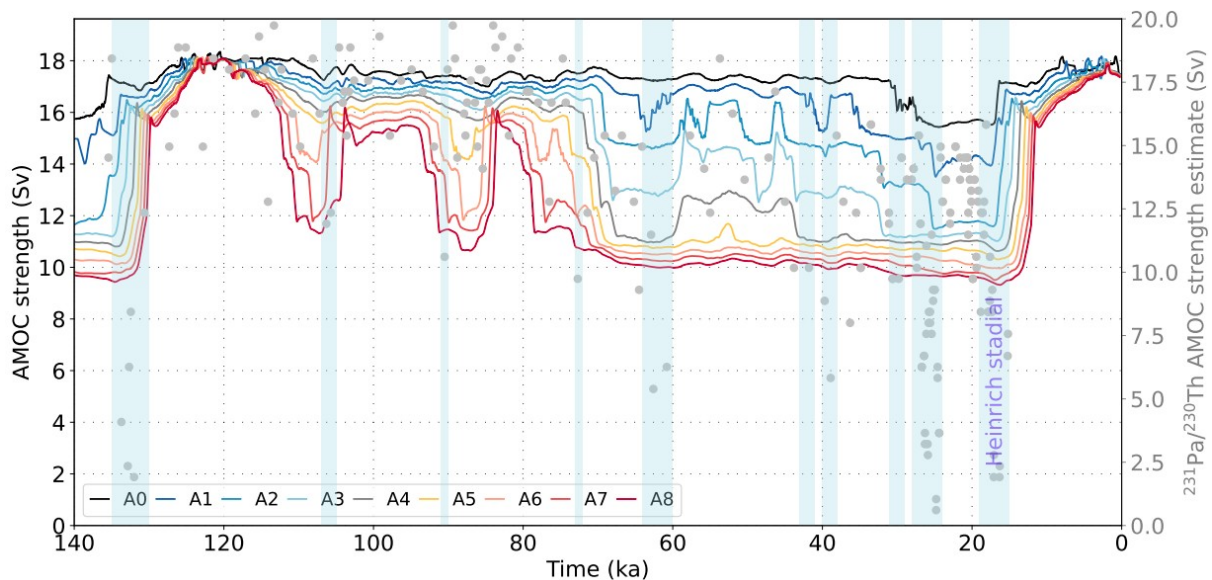
648

649 Figure 8: Simulated AMOC changes due to thermal forcing over the last 140 kyr. Gray dots

650 indicate AMOC strength estimated from ^{231}Pa/^{230}Th (Böhm et al., 2015, Lippold et al., 2009)

651 by assuming a sensitivity of -0.0024 Sv^{-1} (Rempfer et al., 2017).

652

653 Fig. 8 compares the simulated changes in AMOC strength over the last 120 kyr in simulation

654 set A to indications of AMOC weakening based on ^{231}Pa/^{230}Th from the Bermuda Rise (Böhm

655 et al., 2015). The simulations A2-A4 have PI-LGM GMST differences of 4.7-6.2°C (within the

656 proxy-constrained and PMIP range and close to the most recent estimate of 6.1°C by

657 Tierney et al., 2020) and show a shift to a weaker AMOC at the beginning of MIS 4 around

658 70 ka ago, when a negative ^{231}Pa/^{230}Th shift occurred. While the simulated radiation-driven

659 AMOC changes cannot explain weaker or collapsed circulation modes (<11 Sv) during

660 Heinrich stadials, this comparison shows that the long term AMOC weakening during glacial

phases could have been driven by temperature changes. It is important to note that AMOC strength estimates based on this ^{231}Pa/^{230}Th record need to be treated with caution. Pöppelmeier et al. (2021; 2023) showed a strong local influence on sedimentary proxies at this site, and we did not correct the ^{231}Pa/^{230}Th signal for potential productivity changes.

3.4. Meta-stable AMOC modes over the last 788 kyr

Finally, we can test whether our simulations capture the periods with increased frequency of AMOC transitions that are indicated by proxies over the last eight glacial cycles. Using our 788 kyr long simulations in simulation set A, we determined how often and when the radiative forcing pushed the AMOC into 'excitable' circulation modes, i.e. modes II and III, which showed more frequent AMOC strength shifts than the interglacial and glacial modes I and IV (Fig. 1 and SI.2), and how this varied with the applied forcing strength (Fig. 9). In all simulations, the AMOC transitioned into such excitable modes in all of the past eight glacial cycles, but the timing of these shifts varied. For example, during the last glacial cycle, the simulations A2-A4 exhibited an intermediate circulation mode during MIS 3 (57-29 ka), when frequent AMOC mode shifts occurred (see Fig. 1). Similar rapid mode switches occurred earlier in the glacial cycle, i.e. during MIS 5d-e in simulations A6-A8. In these simulations, the AMOC already transitioned into the persistent glacial circulation mode IV at the beginning of MIS 4 (71-57 ka), in which North Atlantic density profiles are more stable. In simulations A1-A3, the AMOC persisted in these modes for several tens of thousands of years at a time, during most glacials. Under stronger radiative forcing, the periods in which AMOC adopted these modes were shorter and mostly occurred at the start of glacial cycles.
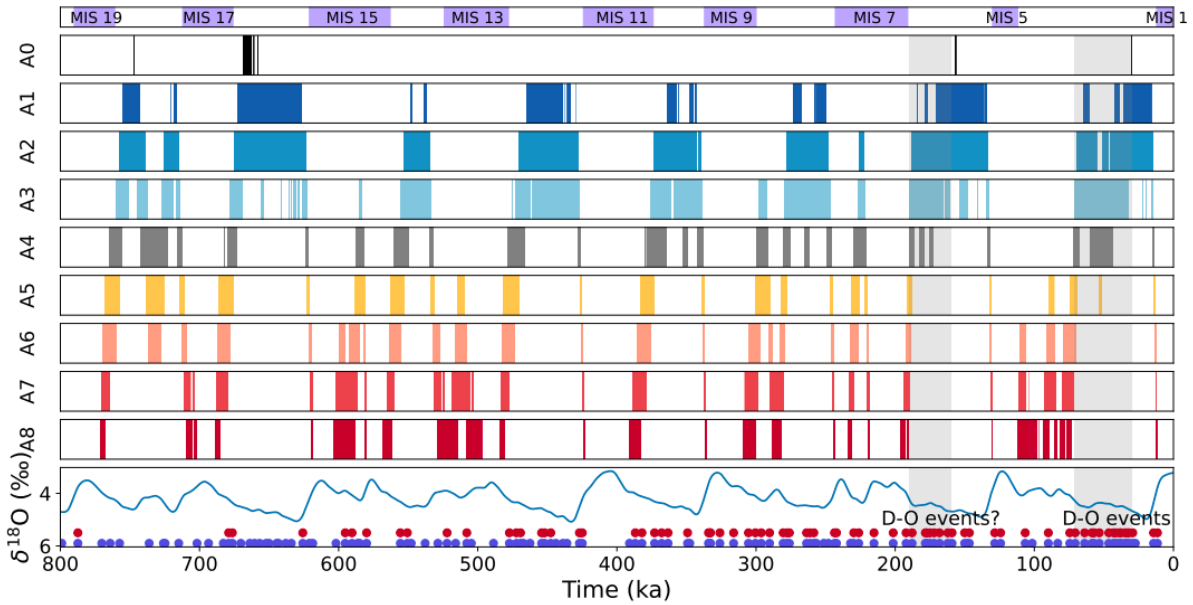
Figure 9: Occurrence of intermediate AMOC modes II and III due to radiative forcing over the last 788 kyr in simulation set A. The time periods with intermediate AMOC modes are marked as vertical bars, each row showing the results for a different forcing magnitude from simulation set A. At the bottom, $\delta^{18}O$ from Lisiecki and Raymo (2005) is shown for reference, alongside the time period with confirmed and suspected Dansgaard-Oeschger events (light gray bars based on Rousseau et al., 2020, blue and red circles are based on reconstructions Barker et al., 2011, who used two different detection thresholds).

We can assess the skill of our simulations at predicting 'excitable' AMOC modes from the radiative forcing by comparing the output with records of high AMOC variability in the past. Simulations A3 and A4 shift into a meta-stable circulation mode during MIS 3, and similarly between 190 and 160 ka during the penultimate glacial cycle, and prior to each previous glacial maximum but not during the glacial maxima themselves. An 'excitable' AMOC mode during these intervals seems realistic given the high frequency of Dansgaard-Oeschger events in MIS 3 and the suspected occurrence of Dansgaard-Oeschger events during MIS 6 (191-123 ka, Rousseau et al. 2020). Similarly, Barker et al. (2011), who predicted the occurrence of Dansgaard-Oeschger events during previous glacial cycles based on the Antarctic methane and temperature records (with two different identification thresholds, red and blue circles in Fig. 9) following the approach of Siddall et al. (2006), found a high frequency of occurrence of Dansgaard-Oeschger events during MIS 3 and 6, but also throughout most other glacial phases. None of our simulations predicts such a ubiquity of 'excitable' AMOC modes, possibly due to the prescribed boundary conditions although the detection method of Barker et al. (2011) is also more uncertain for glacial cycles further back in time. The consistency of the simulated radiation-induced AMOC instability with

710 observational indication of millennial-scale AMOC variability at least during MIS 3 and 6 in
711 simulations A3 and A4 suggests that these could present a more realistic temporal AMOC
712 evolution than the others. Simulations A3 and A4 also exhibit PI-LGM temperature
713 differences of 5.4 and 6.2°C, respectively, close to the proxy-constrained reconstruction
714 (Tierney et al., 2020), and roughly reproduce the reconstructed regional SST changes and
715 reduced circulation strength in MIS 3 and 2 (Fig. 7 and 8).

716

717 Thermal conditioning of AMOC excitability is in line with studies that found the existence of a
718 'sweet spot' in atmospheric CO_2 radiative forcing which is particularly conducive to short,
719 abrupt AMOC perturbations and/or self-sustained AMOC oscillations (e.g. Li and Born, 2019,
720 Vettoretti et al., 2022). Yet, our simulations do not produce such perturbations, partly due to
721 the smoothed forcing and static wind fields (see discussion of model limitations above). The
722 transient circulation mode switches in response to orbitally-paced radiation changes in our
723 simulations are much weaker than those found in other studies (Vettoretti et al., 2022,
724 Klockmann et al., 2018, Kuniyoshi et al., 2022), and our simulations do not contain
725 oscillations that could directly be compared to Dansgaard-Oeschger events.

726

727

728 **4   Conclusions**

729

730 Our study demonstrates the existence of thermal AMOC thresholds and multiple stable
731 circulation modes in the Bern3D model. This adds to previous studies showing that thermal
732 AMOC thresholds emerge in a range of Earth system models varying in complexity and
733 number of components coupled (Zhang et al., 1993), in particular, they also arise in an
734 energetically and hydrologically coupled ocean-sea ice-atmosphere model of intermediate
735 complexity like Bern3D. These thresholds shape the response in the simulated AMOC to
736 radiative orbital and atmospheric composition-driven temperature changes over the last 788
737 kyr. During this period the AMOC transitions between up to four persistent circulation modes.
738 The full glacial and interglacial circulation modes are most frequently simulated, as relatively
739 strong forcing is required to push the AMOC out of them. In contrast, the intermediate AMOC
740 modes are more sensitive to perturbations as small variations in orbital and radiative forcing
741 are able to push the circulation out of these modes. This behaviour resembles the one found
742 in more complex General Circulation Models that exhibit self-sustained oscillations at
743 'sweetspot' CO_2 levels, which lie between glacial and interglacial values. Our simulations
744 suggest that radiative forcing could have created time periods during which highly sensitive
745 intermediate AMOC modes occurred repeatedly over the last 788 kyr.

746

Data availability

All simulation output necessary to produce the figures in this manuscript are available at https://doi.org/10.5281/zenodo.8424878
Proxy data plotted against the simulation output for comparison was taken from public repositories and are available via the citations provided.

Author contributions

AJT ran the simulations. MA analysed the output and drafted the manuscript. All authors contributed to the interpretation of the results and the final manuscript text.

Conflicts of interest

The authors declare that they have no conflict of interest.

Acknowledgements

MA, AJT and FJ were financially supported by the Swiss National Science Foundation

(#200020_200511).

FP was financially supported by the European Union's Horizon 2020 research and innovation programme under grant agreements no. 101023443 (project CliMoTran).

TFS and FP were financially supported by the European Union's Horizon 2020 research and innovation programme under grant agreements no. 820970 (project TiPES), and the Swiss National Science Foundation's project 200020_200492.

Calculations were performed on UBELIX (http://www.id.unibe.ch/hpc), the HPC cluster at the University of Bern.

References

782 **Aeberhardt, M., Blatter, M. and Stocker, T.F., 2000. Variability on the century time**
783 **scale and regime changes in a stochastically forced zonally averaged ocean-**
784 **atmosphere model. Geophysical Research Letters, 27(9), pp.1303-1306.**
785

786 Albani, S., Balkanski, Y., Mahowald, N., Winckler, G., Maggi, V. and Delmonte, B., 2018. Aerosol-
787 climate interactions during the Last Glacial Maximum. *Current Climate Change Reports*, *4*, pp.99-114.
788

789 Ando, T. and Oka, A., 2021. Hysteresis of the glacial Atlantic meridional overturning
790 circulation controlled by thermal feedbacks. Geophysical Research Letters, 48(24),
791 p.e2021GL095809.
792

793 Armstrong, E., Izumi, K. and Valdes, P., 2022. Identifying the mechanisms of DO-scale oscillations in
794 a GCM: a salt oscillator triggered by the Laurentide ice sheet. Climate Dynamics, pp.1-19.
795

796 Arzel, O., England, M.H. and Sijp, W.P., 2008. Reduced stability of the Atlantic meridional overturning
797 circulation due to wind stress feedback during glacial times. Journal of climate, 21(23), pp.6260-6282.
798

799 Banderas, R., Álvarez-Solas, J. and Montoya, M., 2012. Role of CO 2 and Southern Ocean winds in
800 glacial abrupt climate change. Climate of the Past, 8(3), pp.1011-1021.
801

802 Bard, E., Arnold, M., Maurice, P., Duprat, J., Moyes, J. and Duplessy, J.C., 1987. Retreat velocity of
803 the North Atlantic polar front during the last deglaciation determined by 14C accelerator mass
804 spectrometry. *Nature*, *328*(6133), pp.791-794.
805

806 Barker, S., Knorr, G., Edwards, R.L., Parrenin, F., Putnam, A.E., Skinner, L.C., Wolff, E. and Ziegler,
807 M., 2011. 800,000 years of abrupt climate variability. *science*, *334*(6054), pp.347-351.
808

809 Barker, S., Chen, J., Gong, X., Jonkers, L., Knorr, G. and Thornalley, D., 2015. Icebergs not the
810 trigger for North Atlantic cold events. Nature, 520(7547), pp.333-336.
811

812 Bereiter, B., Eggleston, S., Schmitt, J., Nehrbass-Ahles, C., Stocker, T.F., Fischer, H., Kipfstuhl, S.
813 and Chappellaz, J., 2015. Revision of the EPICA Dome C CO2 record from 800 to 600 kyr before
814 present. *Geophysical Research Letters*, *42*(2), pp.542-549.
815

816 Berger, A., 1978. Long-term variations of caloric insolation resulting from the Earth's orbital elements.
817 *Quaternary research*, *9*(2), pp.139-167.
818

819 Berger, A. and Loutre, M.F., 1991. Insolation values for the climate of the last 10 million years.
820 *Quaternary science reviews*, *10*(4), pp.297-317.

821

822 Berger, V.W. and Zhou, Y., 2014. Kolmogorov–smirnov test: Overview. Wiley statsref: Statistics
823 reference online.

824

825 Böhm, E., Lippold, J., Gutjahr, M., Frank, M., Blaser, P., Antz, B., Fohlmeister, J., Frank, N.,
826 Andersen, M.B. and Deininger, M., 2015. Strong and deep Atlantic meridional overturning circulation
827 during the last glacial cycle. *Nature*, *517*(7532), pp.73-76.

828

829 Bouttes, N., Paillard, D., Roche, D.M., Brovkin, V. and Bopp, L., 2011. Last Glacial Maximum CO2
830 and δ13C successfully reconciled. Geophysical Research Letters, 38(2).

831

832 Bozbiyik, A., Steinacher, M., Joos, F., Stocker, T.F. and Menviel, L., 2011. Fingerprints of changes in
833 the terrestrial carbon cycle in response to large reorganizations in ocean circulation. Climate of the
834 Past, 7(1), pp.319-338.

835

836 Broecker, W.S., Blanton, S., Smethie Jr, W.M. and Ostlund, G., 1991. Radiocarbon decay and oxygen
837 utilization in the deep Atlantic Ocean. Global Biogeochemical Cycles, 5(1), pp.87-117.

838

839 Broecker, W.S., 1994. Massive iceberg discharges as triggers for global climate change. *Nature*,
840 *372*(6505), pp.421-424.

841

842 Brown, N. and Galbraith, E.D., 2016. Hosed vs. unhosed: interruptions of the Atlantic Meridional
843 Overturning Circulation in a global coupled model, with and without freshwater forcing. Climate of the
844 Past, 12(8), pp.1663-1679.

845

846 Buizert, C. and Schmittner, A., 2015. Southern Ocean control of glacial AMOC stability and
847 Dansgaard-Oeschger interstadial duration. Paleoceanography, 30(12), pp.1595-1612.

848

849 Candy, I. and Alonso-Garcia, M., 2018. A 1 Ma sea surface temperature record from the North
850 Atlantic and its implications for the early human occupation of Britain. *Quaternary Research*, *90*(2),
851 pp.406-417.

852

853 Dansgaard, W., Johnsen, S.J., Clausen, H.B., Dahl-Jensen, D., Gundestrup, N.S., Hammer, C.U.,
854 Hvidberg, C.S., Steffensen, J.P., Sveinbjörnsdottir, A.E., Jouzel, J. and Bond, G., 1993. Evidence for
855 general instability of past climate from a 250-kyr ice-core record. *nature*, *364*(6434), pp.218-220.

856

857 Davtian, N. and Bard, E., 2023. A new view on abrupt climate changes and the bipolar seesaw based
858 on paleotemperatures from Iberian Margin sediments. *Proceedings of the National Academy of*
859 *Sciences*, *120*(12), p.e2209558120.

860

De Boer, A.M., Gnanadesikan, A., Edwards, N.R. and Watson, A.J., 2010. Meridional density gradients do not control the Atlantic overturning circulation. *Journal of Physical Oceanography*, *40*(2), pp.368-380.

de Vries, P. and Weber, S.L., 2005. The Atlantic freshwater budget as a diagnostic for the existence of a stable shut down of the meridional overturning circulation. Geophysical Research Letters, 32(9).

Edwards, N. R., Willmott, A. J., and Killworth, P. D.: On the role of topography and wind stress on the stability of the thermohaline circulation, J. Phys. Oceanogr., 28, 756–778, https://doi.org/10.1175/1520-0485(1998)028<0756:OTROTA>2.0.CO;2, 1998.

Fischer, H., Meissner, K.J., Mix, A.C., Abram, N.J., Austermann, J., Brovkin, V., Capron, E., Colombaroli, D., Daniau, A.L., Dyez, K.A. and Felis, T., 2018. Palaeoclimate constraints on the impact of 2 C anthropogenic warming and beyond. *Nature geoscience*, *11*(7), pp.474-485.

Galbraith, E. and de Lavergne, C., 2019. Response of a comprehensive climate model to a broad range of external forcings: relevance for deep ocean ventilation and the development of late Cenozoic ice ages. Climate Dynamics, 52, pp.653-679.

Ganopolski, A. and Rahmstorf, S., 2001. Rapid changes of glacial climate simulated in a coupled climate model. Nature, 409(6817), pp.153-158.

Gregory, J.M., Dixon, K.W., Stouffer, R.J., Weaver, A.J., Driesschaert, E., Eby, M., Fichefet, T., Hasumi, H., Hu, A., Jungclaus, J.H. and Kamenkovich, I.V., 2005. A model intercomparison of changes in the Atlantic thermohaline circulation in response to increasing atmospheric CO2 concentration. Geophysical Research Letters, 32(12).

Griffies, S. M.: The Gent–McWilliams Skew Flux, J. Phys. Oceanogr., 28, 831–841, https://doi.org/10.1175/1520-0485(1998)028<0831:TGMSF>2.0.CO;2, 1998.

Grousset, F.E., Pujol, C., Labeyrie, L., Auffret, G. and Boelaert, A., 2000. Were the North Atlantic Heinrich events triggered by the behavior of the European ice sheets?. *Geology*, *28*(2), pp.123-126.

Haskins, R.K., Oliver, K.I., Jackson, L.C., Wood, R.A. and Drijfhout, S.S., 2020. Temperature domination of AMOC weakening due to freshwater hosing in two GCMs. Climate Dynamics, 54, pp.273-286.

Heinrich, H., 1988. Origin and consequences of cyclic ice rafting in the northeast Atlantic Ocean during the past 130,000 years. *Quaternary research*, *29*(2), pp.142-152.

901 Hu, A., Meehl, G.A., Han, W., Timmermann, A., Otto-Bliesner, B., Liu, Z., Washington, W.M., Large,
902 W., Abe-Ouchi, A., Kimoto, M. and Lambeck, K., 2012. Role of the Bering Strait on the hysteresis of
903 the ocean conveyor belt circulation and glacial climate stability. Proceedings of the National Academy
904 of Sciences, 109(17), pp.6417-6422.

906 Ivanovic, R.F., Valdes, P.J., Gregoire, L., Flecker, R. and Gutjahr, M., 2014. Sensitivity of modern
907 climate to the presence, strength and salinity of Mediterranean-Atlantic exchange in a global general
908 circulation model. Climate dynamics, 42, pp.859-877.

910 Jackson, L.C., Schaller, N., Smith, R.S., Palmer, M.D. and Vellinga, M., 2014. Response of the
911 Atlantic meridional overturning circulation to a reversal of greenhouse gas increases. Climate
912 dynamics, 42, pp.3323-3336.

914 Jackson, L.C. and Wood, R.A., 2018. Hysteresis and resilience of the AMOC in an eddy-permitting
915 GCM. *Geophysical Research Letters*, *45*(16), pp.8547-8556.

917 Jackson, L.C., Alastrué de Asenjo, E., Bellomo, K., Danabasoglu, G., Haak, H., Hu, A., Jungclaus,
918 J.H., Lee, W., Meccia, V.L., Saenko, O. and Shao, A., 2023. Understanding AMOC stability: the North
919 Atlantic hosing model intercomparison project. Geoscientific Model Development, 16, pp.1975-1995.

921 Johnson, H.L., Cessi, P., Marshall, D.P., Schloesser, F. and Spall, M.A., 2019. Recent contributions of
922 theory to our understanding of the Atlantic meridional overturning circulation. *Journal of Geophysical
923 Research: Oceans*, *124*(8), pp.5376-5399.

925 Joos, F. and Spahni, R., 2008. Rates of change in natural and anthropogenic radiative forcing over
926 the past 20,000 years. *Proceedings of the National Academy of Sciences*, *105*(5), pp.1425-1430.

928 Joos, H., Madonna, E., Witlox, K., Ferrachat, S., Wernli, H. and Lohmann, U., 2017. Effect of
929 anthropogenic aerosol emissions on precipitation in warm conveyor belts in the western North Pacific
930 in winter–a model study with ECHAM6-HAM. Atmospheric chemistry and physics, 17(10), pp.6243-
931 6255.

933 Kageyama, M., Harrison, S.P., Kapsch, M.L., Lofverstrom, M., Lora, J.M., Mikolajewicz, U., Sherriff-
934 Tadano, S., Vadsaria, T., Abe-Ouchi, A., Bouttes, N. and Chandan, D., 2021. The PMIP4 Last Glacial
935 Maximum experiments: preliminary results and comparison with the PMIP3 simulations. *Climate of the
936 Past*, *17*(3), pp.1065-1089.

938 Klockmann, M., Mikolajewicz, U. and Marotzke, J., 2018. Two AMOC states in response to
939 decreasing greenhouse gas concentrations in the coupled climate model MPI-ESM. Journal of
940 Climate, 31(19), pp.7969-7984.

941

942 Klockmann, M., Mikolajewicz, U., Kleppin, H. and Marotzke, J., 2020. Coupling of the subpolar gyre
943 and the overturning circulation during abrupt glacial climate transitions. Geophysical Research
944 Letters, 47(21), p.e2020GL090361.

945

946 Knorr, G. and Lohmann, G., 2007. Rapid transitions in the Atlantic thermohaline circulation triggered
947 by global warming and meltwater during the last deglaciation. Geochemistry, Geophysics,
948 Geosystems, 8(12).

949

950 Knutti, R. and Stocker, T.F., 2002. Limited predictability of the future thermohaline circulation close to
951 an instability threshold. Journal of Climate, 15(2), pp.179-186.

952

953 Kuniyoshi, Y., Abe-Ouchi, A., Sherriff-Tadano, S., Chan, W.L. and Saito, F., 2022. Effect of Climatic
954 Precession on Dansgaard-Oeschger-Like Oscillations. *Geophysical Research Letters*, *49*(6),
955 p.e2021GL095695.

956

957 Li, C. and Born, A., 2019. Coupled atmosphere-ice-ocean dynamics in Dansgaard-Oeschger events.
958 Quaternary Science Reviews, 203, pp.1-20.

959

960 Lippold, J., Grützner, J., Winter, D., Lahaye, Y., Mangini, A. and Christl, M., 2009. Does sedimentary
961 231Pa/230Th from the Bermuda Rise monitor past Atlantic meridional overturning circulation?.
962 *Geophysical Research Letters*, *36*(12).

963

964 Lisiecki, L. E. & Raymo, M. E. A, 2005. Pliocene-Pleistocene stack of 57 globally distributed benthic
965 d18O records. Paleoceanography 20, PA1003, doi:10.1029/ 2004PA001071.

966

967 Lisiecki, L.E. and Stern, J.V., 2016. Regional and global benthic δ18O stacks for the last glacial cycle.
968 *Paleoceanography*, *31*(10), pp.1368-1394.

969

970 Liu, W., Xie, S.P., Liu, Z. and Zhu, J., 2017. Overlooked possibility of a collapsed Atlantic Meridional
971 Overturning Circulation in warming climate. *Science Advances*, *3*(1), p.e1601666.

972

973 Lohmann, J., Dijkstra, H.A., Jochum, M., Lucarini, V. and Ditlevsen, P.D., 2023. Multistability and
974 Intermediate Tipping of the Atlantic Ocean Circulation. arXiv preprint arXiv:2304.05664.

975

976 Loulergue, L., Schilt, A., Spahni, R., Masson-Delmotte, V., Blunier, T., Lemieux, B., Barnola, J.M.,
977 Raynaud, D., Stocker, T.F. and Chappellaz, J., 2008. Orbital and millennial-scale features of
978 atmospheric CH4 over the past 800,000 years. *Nature*, *453*(7193), pp.383-386.

979

980 Lynch-Stieglitz, J., 2017. The Atlantic meridional overturning circulation and abrupt climate change.
981 *Annual review of marine science*, *9*, pp.83-104.

982

983 Malmierca-Vallet, Irene, Louise C. Sime and the D-O community members. "Dansgaard-Oeschger
984 events in climate models: Review and baseline MIS3 protocol." *Climate of the Past*, *19*(5), pp.915-
985 942.

986

987 Manabe, S. and Stouffer, R.J., 1993. Century-scale effects of increased atmospheric C02 on the
988 ocean–atmosphere system. Nature, 364(6434), pp.215-218.

989

990 Masson-Delmotte, V., Schulz, M., Abe-Ouchi, A., Beer, J., Ganopolski, A., González Rouco, J.F.,
991 Jansen, E., Lambeck, K., Luterbacher, J., Naish, T. and Osborn, T., 2013. Information from
992 paleoclimate archives. In IPCC AR5 Climate Change 2013 - The Physical Science Basis (eds
993 Stocker, T. et al.), *383464*, p.2013.

994

995 Menary, M.B., Roberts, C.D., Palmer, M.D., Halloran, P.R., Jackson, L., Wood, R.A., Müller, W.A.,
996 Matei, D. and Lee, S.K., 2013. Mechanisms of aerosol-forced AMOC variability in a state of the art
997 climate model. Journal of Geophysical Research: Oceans, 118(4), pp.2087-2096.

998

999 Menviel, L., Timmermann, A., Mouchet, A. and Timm, O., 2008. Meridional reorganizations of marine
1000 and terrestrial productivity during Heinrich events. Paleoceanography, 23(1).

1001

1002 Menviel, L., Joos, F. and Ritz, S.P., 2012. Simulating atmospheric CO2, 13C and the marine carbon
1003 cycle during the Last Glacial–Interglacial cycle: possible role for a deepening of the mean
1004 remineralization depth and an increase in the oceanic nutrient inventory. Quaternary Science
1005 Reviews, 56, pp.46-68.

1006

1007 Mikolajewicz, U., Santer, B.D. and Maier-Reimer, E., 1990. Ocean response to greenhouse warming.
1008 Nature, 345(6276), pp.589-593.

1009

1010 Müller, S.A., Joos, F., Edwards, N.R. and Stocker, T.F., 2006. Water mass distribution and ventilation
1011 time scales in a cost-efficient, three-dimensional ocean model. Journal of Climate, 19(21), pp.5479-
1012 5499.

1013

1014 Oeschger, H., Beer, J., Siegenthaler, U., Stauffer, B., Dansgaard, W. and Langway, C.C., 1984. Late
1015 glacial climate history from ice cores. *Climate processes and climate sensitivity*, *29*, pp.299-306.

1016

1017 Oka, A., Hasumi, H. and Abe-Ouchi, A., 2012. The thermal threshold of the Atlantic meridional
1018 overturning circulation and its control by wind stress forcing during glacial climate. Geophysical
1019 Research Letters, 39(9).

Oka, A., Abe-Ouchi, A., Sherriff-Tadano, S., Yokoyama, Y., Kawamura, K. and Hasumi, H., 2021. Glacial mode shift of the Atlantic meridional overturning circulation by warming over the Southern Ocean. Communications Earth & Environment, 2(1), p.169.

Okazaki, Y., Timmermann, A., Menviel, L., Harada, N., Abe-Ouchi, A., Chikamoto, M.O., Mouchet, A. and Asahi, H., 2010. Deepwater formation in the North Pacific during the last glacial termination. Science, 329(5988), pp.200-204.

Pedro, J.B., Jochum, M., Buizert, C., He, F., Barker, S. and Rasmussen, S.O., 2018. Beyond the bipolar seesaw: Toward a process understanding of interhemispheric coupling. Quaternary Science Reviews, 192, pp.27-46.

Pöppelmeier, F., Scheen, J., Jeltsch-Thömmes, A. and Stocker, T.F., 2020. Simulated stability of the AMOC during the Last Glacial Maximum under realistic boundary conditions. *Climate of the Past*, *2021 17, no. 2 (2021): 615-632.*

Pöppelmeier, F., Scheen, J., Jeltsch-Thömmes, A. and Stocker, T.F., 2021. Simulated stability of the Atlantic meridional overturning circulation during the Last Glacial Maximum. Climate of the Past, 17(2), pp.615-632.

Pöppelmeier, F., Jeltsch-Thömmes, A., Lippold, J., Joos, F. and Stocker, T.F., 2023. Multi-proxy constraints on Atlantic circulation dynamics since the last ice age. *Nature geoscience*, *16*(4), pp.349-356.

Praetorius, S.K. and Mix, A.C., 2014. Synchronization of North Pacific and Greenland climates preceded abrupt deglacial warming. Science, 345(6195), pp.444-448.

Rahmstorf, S., 1996. On the freshwater forcing and transport of the Atlantic thermohaline circulation, Clim. Dyn., 12, 799–811.

Rahmstorf, S., 1998. Influence of Mediterranean outflow on climate. Eos, Transactions American Geophysical Union, 79(24), pp.281-282.

Rempfer, J., Stocker, T.F., Joos, F., Lippold, J. and Jaccard, S.L., 2017. New insights into cycling of 231Pa and 230Th in the Atlantic Ocean. *Earth and Planetary Science Letters*, *468*, pp.27-37.

Ritz, S.P., Stocker, T.F. and Joos, F., 2011. A coupled dynamical ocean–energy balance atmosphere model for paleoclimate studies. Journal of Climate, 24(2), pp.349-375.

1060 Roth, R., Ritz, S. P., and Joos, F., 2014: Burial-nutrient feedbacks amplify the sensitivity of
1061 atmospheric carbon dioxide to changes in organic matter remineralisation, Earth Syst. Dynam., 5,
1062 321–343.

1064 Rousseau, D.D., Antoine, P., Boers, N., Lagroix, F., Ghil, M., Lomax, J., Fuchs, M., Debret, M., Hatté,
1065 C., Moine, O. and Gauthier, C., 2020. Dansgaard–Oeschger-like events of the penultimate climate
1066 cycle: the loess point of view. *Climate of the Past*, *16*(2), pp.713-727.

1068 Ruddiman, W.F. and McIntyre, A., 1981. The North Atlantic Ocean during the last deglaciation.
1069 *Palaeogeography, Palaeoclimatology, Palaeoecology*, *35*, pp.145-214.

1071 Severinghaus, J.P., Beaudette, R., Headly, M.A., Taylor, K. and Brook, E.J., 2009. Oxygen-18 of O2
1072 records the impact of abrupt climate change on the terrestrial biosphere. Science, 324(5933),
1073 pp.1431-1434.

1075 Sherriff-Tadano, S. and Klockmann, M., 2021. PmiP contributions to understanding the deep ocean
1076 circulation of the last glacial maximum. *Past Global Changes Magazine*, *29*(2), pp.84-85.

1078 Sherriff-Tadano, S., Abe-Ouchi, A., Yoshimori, M., Ohgaito, R., Vadsaria, T., Chan, W.L., Hotta, H.,
1079 Kikuchi, M., Kodama, T., Oka, A. and Suzuki, K., 2023. Southern Ocean surface temperatures and
1080 cloud biases in climate models connected to the representation of glacial deep ocean circulation.
1081 Journal of Climate, 36(11), pp.3849-3866.

1083 Siddall, M., T.F. Stocker, T. Blunier, R. Spahni, J. McManus, and E. Bard, Using a maximum simplicity
1084 paleoclimate model to simulate millennial variability during the last four glacial periods, Quat. Sci.
1085 Rev., 25, 3185-3197, 2006.

1087 Stocker, T.F., and D.G. Wright, Rapid transitions of the ocean's deep circulation induced by changes
1088 in surface water fluxes, Nature, 351, 729-732, 1991.

1090 Stocker, T.F. and Schmittner, A., 1997. Influence of CO_2 emission rates on the stability of the
1091 thermohaline circulation. Nature, 388(6645), pp.862-865.

1093 Stocker, T.F., 2000. Past and future reorganizations in the climate system. Quaternary Science
1094 Reviews, 19(1-5), pp.301-319.

1096 Stocker, T.F. and Johnsen, S.J., 2003. A minimum thermodynamic model for the bipolar seesaw.
1097 Paleoceanography, 18(4).

1099   Stommel, H., 1961. Thermohaline convection with two stable regimes of flow. Tellus, 13(2), 224– 230.
1100   https://doi.org/10.3402/tellusb.v13i2.12985

1102   Swingedouw, D., Colin, C., Eynaud, F., Ayache, M. and Zaragosi, S., 2019. Impact of freshwater
1103   release in the Mediterranean Sea on the North Atlantic climate. Climate Dynamics, 53, pp.3893-3915.

1105   Swingedouw, D., Houssais, M.N., Herbaut, C., Blaizot, A.C., Devilliers, M. and Deshayes, J., 2022.
1106   AMOC Recent and Future Trends: A Crucial Role for Oceanic Resolution and Greenland Melting?.
1107   *Frontiers in Climate*, p.32.

1109   Tetard, M., Licari, L. and Beaufort, L., 2017. Oxygen history off Baja California over the last 80 kyr: A
1110   new foraminiferal-based record. Paleoceanography, 32(3), pp.246-264.

1112   Tierney, J.E., Zhu, J., King, J., Malevich, S.B., Hakim, G.J. and Poulsen, C.J., 2020. Glacial cooling
1113   and climate sensitivity revisited. *Nature*, *584*(7822), pp.569-573.

1115   Timmermann, A. and Friedrich, T., 2016. Late Pleistocene climate drivers of early human migration.
1116   Nature, 538(7623), pp.92-95.

1118   Vettoretti, G., Ditlevsen, P., Jochum, M. and Rasmussen, S.O., 2022. Atmospheric CO2 control of
1119   spontaneous millennial-scale ice age climate oscillations. Nature Geoscience, 15(4), pp.300-306.

1121   Wang, Y.J., Cheng, H., Edwards, R.L., An, Z.S., Wu, J.Y., Shen, C.C. and Dorale, J.A., 2001. A high-
1122   resolution absolute-dated late Pleistocene monsoon record from Hulu Cave, China. Science,
1123   294(5550), pp.2345-2348.

1125   Weijer, W., Cheng, W., Drijfhout, S.S., Fedorov, A.V., Hu, A., Jackson, L.C., Liu, W., McDonagh, E.L.,
1126   Mecking, J.V. and Zhang, J., 2019. Stability of the Atlantic Meridional Overturning Circulation: A
1127   review and synthesis. *Journal of Geophysical Research: Oceans*, *124*(8), pp.5336-5375.

1129   Weijer, W., Cheng, W., Garuba, O.A., Hu, A. and Nadiga, B.T., 2020. CMIP6 models predict
1130   significant 21st century decline of the Atlantic meridional overturning circulation. Geophysical
1131   Research Letters, 47(12), p.e2019GL086075.

1133   Winckler, G., Anderson, R.F., Fleisher, M.Q., McGee, D. and Mahowald, N., 2008. Covariant glacial-
1134   interglacial dust fluxes in the equatorial Pacific and Antarctica. science, 320(5872), pp.93-96.

1136   Yang, H., Wang, K., Dai, H., Wang, Y. and Li, Q., 2016. Wind effect on the Atlantic meridional
1137   overturning circulation via sea ice and vertical diffusion. Climate Dynamics, 46, pp.3387-3403.
1138

1139 Zhang, S., Greatbatch, R.J. and Lin, C.A., 1993. A reexamination of the polar halocline catastrophe
1140 and implications for coupled ocean-atmosphere modeling. Journal of Physical Oceanography, 23(2),
1141 pp.287-299.

1143 Zhang, X., Prange, M., Merkel, U. and Schulz, M., 2014. Instability of the Atlantic overturning
1144 circulation during Marine Isotope Stage 3. Geophysical Research Letters, 41(12), pp.4285-4293.

1146 Zhang, X., Knorr, G., Lohmann, G. and Barker, S., 2017. Abrupt North Atlantic circulation changes in
1147 response to gradual CO2 forcing in a glacial climate state. Nature Geoscience, 10(7), pp.518-523.
1148